

Nutraceuticals in Bulk and Dosage Forms: Analysis by ^{35}Cl and ^{14}N Solid-State NMR and DFT Calculations

Sean T. Holmes, James M. Hook, and Robert W. Schurko*

Cite This: <https://doi.org/10.1021/acs.molpharmaceut.1c00708>

Read Online

ACCESS |



Metrics & More



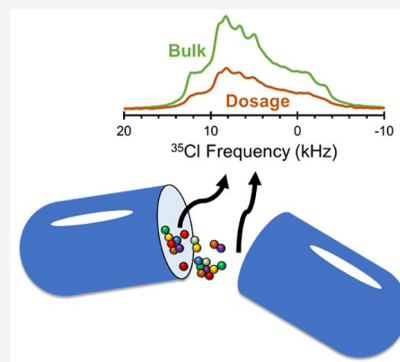
Article Recommendations



Supporting Information

ABSTRACT: This study uses ^{35}Cl and ^{14}N solid-state NMR (SSNMR) spectroscopy and dispersion-corrected plane-wave density functional theory (DFT) calculations for the structural characterization of chloride salts of nutraceuticals in their bulk and dosage forms. For eight nutraceuticals, we measure the ^{35}Cl EFG tensor parameters of the chloride ions and use plane-wave DFT calculations to elucidate relationships between NMR parameters and molecular-level structure, which provide rapid NMR crystallographic assessments of structural features. We employ both ^{35}Cl direct excitation and $^1\text{H}\rightarrow^{35}\text{Cl}$ cross-polarization methods to characterize a dosage form containing α -D-glucosamine HCl, observe possible impurity and/or adulterant phases, and quantify the weight percent of the active ingredient. To complement this, we also investigate ^{14}N SSNMR spectroscopy and DFT calculations to characterize nitrogen atoms in the nutraceuticals. This includes a discussion of targeted acquisition experimental protocols (i.e., acquiring a select region of the overall pattern that features key discontinuities) that allow ultrawide-line spectra to be acquired rapidly, even for unresponsive samples (i.e., those with long values of $T_1(^{14}\text{N})$, short values of $T_2^{\text{eff}}(^{14}\text{N})$, or very broad patterns). It is hoped that these experimental and computational protocols will be useful for the characterization of various solid forms of nutraceuticals (i.e., salts, polymorphs, hydrates, solvates, cocrystals, amorphous solid dispersions, etc.), help detect impurity and counterfeit solid phases in dosage forms, and serve as a foundation for future NMR crystallographic studies of nutraceutical solid forms, including studies using *ab initio* crystal structure prediction algorithms.

KEYWORDS: nutraceuticals, dosage forms, glucosamine, NMR, nuclear magnetic resonance, electric field gradients, nitrogen, chlorine, density functional theory, DFT



1. INTRODUCTION

Nutraceuticals are defined variously as pharmaceutical-grade nutrients or pharmaceutical alternatives, and include dietary supplements and functional foods, or their isolated active ingredients (as used in the context of the present work), which are administered in a medicinal form.^{1–3} The nutraceutical industry is expanding rapidly, with an estimated global market size of ca. 380 billion USD in 2019, and a forecasted compound annual growth rate of 8.3% percent between 2020–2027.⁴

Nutraceutical oral dosage forms are often manufactured, stored, and ingested as crystalline or amorphous solids. The physicochemical properties of nutraceuticals, including their stability, solubility, bioavailability, and reactivity, depend on the nature of the solid in the dosage form;⁵ thus, the design and manufacture of novel nutraceutical solid forms that modulate these properties is an important area within both crystal engineering and pharmaceutical science. Common solid forms of nutraceuticals include salts, polymorphs, hydrates, solvates, cocrystals (including drug-nutraceutical cocrystals), amorphous solid dispersions, and combinations thereof.^{6–13} For these reasons, it is critical to develop methods for characterizing the molecular-level structures of nutraceutical

solid forms, quantifying nutraceuticals in dosage forms, and even detecting impurities, adulterants, or counterfeited nutraceutical products.¹⁴

Hydrochloride (HCl) salts are among the most common solid forms of nutraceuticals.¹⁵ HCl salts are stabilized by intermolecular noncovalent interactions, most notably hydrogen bonding, between nutraceutical molecules and chloride ions;^{16,17} hence, the development of robust techniques for the characterization of the local hydrogen-bonding environments of the chloride ions and key organic moieties is of great importance.

There are many techniques used to characterize nutraceuticals, including powder and single-crystal X-ray diffraction (PXRD and SCXRD, respectively), thermal analysis, dynamic vapor sorption, vibrational spectroscopy, and solid-state NMR (SSNMR) spectroscopy.¹⁸ Of these techniques, only SSNMR

Special Issue: Crystallizing the Role of Solid-State Form in Drug Delivery

Received: September 9, 2021

Revised: November 3, 2021

Accepted: November 5, 2021

provides site-specific information on molecular-level structure and dynamics in nutraceuticals in their bulk and dosage forms (*vide infra*). Herein, we use ^{35}Cl and ^{14}N multinuclear SSNMR to characterize the molecular-level structures of HCl salts of nutraceuticals with an emphasis on characterizing hydrogen-bonding interactions and their influences on NMR spectra, as well as for the use of such information for the refinement of crystal structures.

The central transition (CT, $+1/2 \leftrightarrow -1/2$) powder patterns observed in ^{35}Cl ($I = 3/2$) SSNMR spectra, which can manifest the effects of both the second-order quadrupolar interaction (SOQI) and chlorine chemical shift anisotropy (CSA), reflect subtle differences and/or changes between local environments of chloride ions, making ^{35}Cl SSNMR spectroscopy an important method for characterizing networks of hydrogen bonds involving nitrogen- and oxygen-containing moieties that stabilize solid forms of organic HCl salts involving active pharmaceutical ingredients (APIs) and nutraceuticals.^{19–45} Another advantage of ^{35}Cl SSNMR is its applicability to the characterization of API and nutraceuticals in their dosage forms; this characteristic is distinctive of ^{35}Cl SSNMR spectroscopy because the spectra obtained by many common NMR techniques and nuclides (i.e., ^1H , ^{13}C , ^{15}N) are complicated by the presence of signals arising from excipient molecules, making their interpretation difficult or impossible (especially if the concentration or weight percent of the active ingredient is low).^{23,24,44,45} Accordingly, ^{35}Cl SSNMR spectroscopy is anticipated to play an important role in the structural characterization and fingerprinting of nutraceuticals in their bulk and dosage forms, as well as for quantification and detection of impurities, adulterants, and counterfeit products; each of these considerations is relevant to both consumers and manufacturers of nutraceuticals.^{46,47}

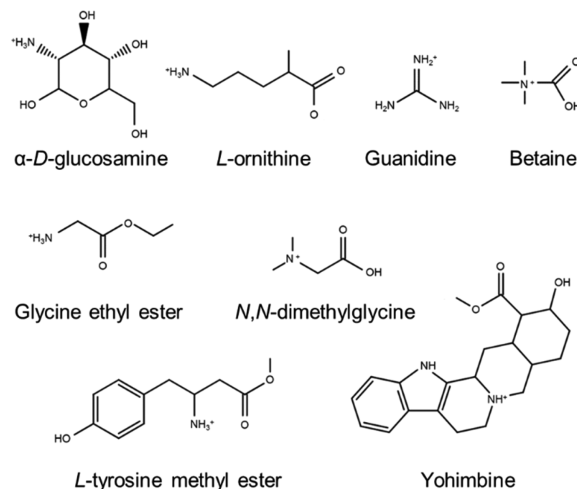
^{14}N powder patterns, which are generally dominated by the first-order quadrupolar interaction (FOQI) and exhibit the characteristic Pake-like doublet shape resulting from the overlap of two satellite transition (ST) powder patterns arising from fundamental $0 \leftrightarrow -1$ and $+1 \leftrightarrow 0$ transitions, can provide additional insight into the nature of hydrogen bonding networks in nutraceuticals.^{48–50} When nitrogen-containing moieties act as hydrogen-bond donors in HCl salts, the $\text{N}\cdots\text{H}\cdots\text{Cl}^-$ bonds influence the nitrogen EFG tensors, as well as the appearances of ^{14}N SSNMR spectra. However, ^{14}N patterns are typically very broad, with breadths ranging from hundreds of kHz to several MHz. For pseudotetrahedral nitrogen moieties, such as those present in many nutraceuticals, pattern breadths generally exceed 1.0 MHz and are known to be as broad as ca. 2.25 MHz.^{49,51–55} Consequently, the acquisition of ^{14}N ultrawideband (UW) NMR spectra requires the use of specialized pulses and pulse sequences that are designed for broadband excitation, refocusing, and cross-polarization.^{49–59} Thus, in addition to using ^{14}N SSNMR for the structural characterization of nutraceuticals, we are interested in developing efficient methodologies for acquiring UW ^{14}N SSNMR spectra from which one can determine nitrogen EFG tensor parameters. Of particular use is the targeted acquisition of select regions of UW NMR spectra that feature key discontinuities, which provides a means of measuring ^{14}N EFG tensor parameters without any significant loss of precision.⁵⁰

Plane-wave DFT calculations are useful for interpreting relationships between nuclear EFG tensors and molecular-level structure.^{60–62} Because ^{35}Cl EFG tensors are influenced

strongly by the geometries of hydrogen bonding networks, DFT calculations are useful for assessing the validity of crystal structures using comparison of experimentally measured and theoretically derived NMR interaction tensors as benchmarks. Similarly, the effects of hydrogen bonding are evident in the calculation of ^{14}N EFG tensors, although these tend to be proportionately smaller because the local electronic structures of nitrogen atoms are normally dominated by the effects of covalent bonding, rather than hydrogen bonding. To assess the relationships between EFG tensors and molecular-level structure, our research group has developed semiempirical dispersion-corrected force field models, used in the context of plane-wave DFT calculations, which are optimized for the refinement of the structures of organic solids, the calculation of EFG and chemical shift tensors, and the elucidation of relationships between NMR spectra and molecular-level structure and dynamics.^{60–63} More so than other DFT-based structural refinement protocols, these methods result in accurate calculations of EFG and chemical shift tensors (which have independent electric and magnetic origins, respectively), as well as sets of atomic coordinates that are comparable to those obtained from neutron diffraction methods.^{60,62}

In this work, we present a multinuclear SSNMR and DFT approach for characterizing nutraceuticals in their bulk and dosage forms (Scheme 1). First, we use ^{35}Cl SSNMR spectra

Scheme 1. Cationic Molecular Structures of Nutraceuticals



obtained at two fields, under static and magic-angle spinning (MAS) conditions, to characterize the ^{35}Cl EFG and chemical shift tensors of chloride ions in eight nutraceuticals. Dispersion-corrected plane-wave DFT calculations are used to refine the crystal structures of the nutraceuticals and provide key relationships between the local environments of the chloride ion and the ^{35}Cl EFG tensor parameters. Second, we use ^{35}Cl direct excitation (DE) and $^1\text{H} \rightarrow ^{35}\text{Cl}$ cross-polarization (CP) NMR techniques to characterize a tablet containing α -D-glucosamine HCl and quantify its weight percent (wt %). Third, we use ^{14}N SSNMR spectroscopy and DFT calculations to characterize nitrogen atoms in the nutraceuticals; this includes a discussion of experimental protocols that allow UW ^{14}N spectra of organic solids to be acquired rapidly and efficiently.⁵⁰ Finally, we discuss how these experimental and computational protocols can be used for the characterization of various solid forms of nutraceuticals, laying

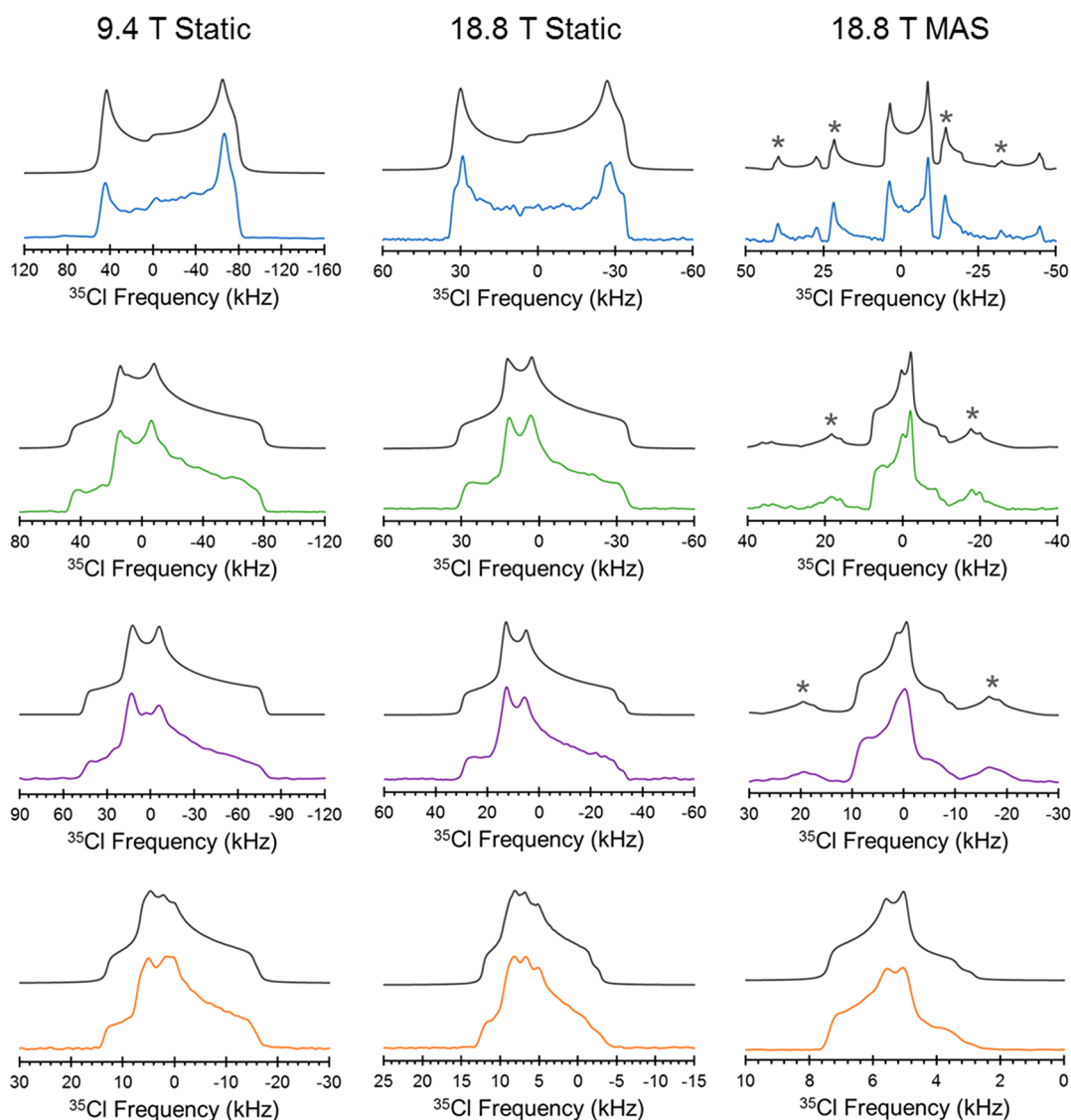


Figure 1. Experimental $^{35}\text{Cl}\{^1\text{H}\}$ SSNMR spectra of betaine HCl (blue), *N,N*-dimethylglycine HCl (green), yohimbine HCl (purple), α -D-glucosamine HCl (orange), and corresponding analytical simulations (gray). Spectra of static samples were acquired at 9.4 and 18.8 T, and under MAS conditions at 18.8 T. Spinning side bands are marked by asterisks (*).

the groundwork for further studies on nutraceuticals in areas of NMR crystallography, identification of polymorphs, and rapid spectral fingerprinting for the purpose of detecting counterfeits.

2. EXPERIMENTAL AND COMPUTATIONAL DETAILS

2.1. Materials. All bulk phase samples were purchased from MilliporeSigma and used without further purification. The identities of the bulk materials were confirmed through comparison with simulated PXRD patterns based on previously reported crystal structures; these results indicate that each nutraceutical is highly crystalline, and no impurity phases are evident (Figure S1, see Supporting Information).^{64–71} Schiff Glucosamine (Schiff Nutrition International) tablets were purchased from Publix Super Markets, Inc., which were stated to contain 500 mg α -D-glucosamine HCl, 500 mg methylsulfonylmethane, 1.1 mg hyaluronic acid, an unspecified quantity of additional excipients (hydroxypropyl cellulose, silicon dioxide, magnesium stearate, and boron glycinate), and coatings (hydroxypropyl methylcellulose, modified corn starch,

titanium dioxide, polyethylene glycol, glycerin, and magnesium silicate) per tablet.

2.2. Powder X-ray Diffraction. PXRD patterns were acquired with a Rigaku Miniflex X-ray diffractometer operating with Bragg–Brentano geometry and featuring a Cu $K\alpha$ ($\lambda = 1.540593 \text{ \AA}$) radiation source and a D/tex Ultra 250 1D silicon strip detector. The X-ray tube voltage and amperage were 40 kV and 15 mA, respectively. Samples were packed in zero-background silicon wafers with a well size of 5 mm \times 0.2 mm mounted on an eight-position autosampler. Diffraction patterns were acquired with a detector scanning 2θ from 5° to 50° with a step size of 0.03° at a rate of 5° min^{-1} . Simulated diffraction patterns were generated using the Mercury software package.⁷²

2.3. Solid-State NMR Spectroscopy. Overview. All NMR data at a field strength of 9.4 T were obtained at the University of Windsor (Windsor, Ontario, Canada) using a Bruker Avance III HD spectrometer and an Oxford wide bore magnet, with Larmor frequencies of $\nu_0(^1\text{H}) = 399.73 \text{ MHz}$ and $\nu_0(^{35}\text{Cl}) = 39.26 \text{ MHz}$. These spectra were acquired with a

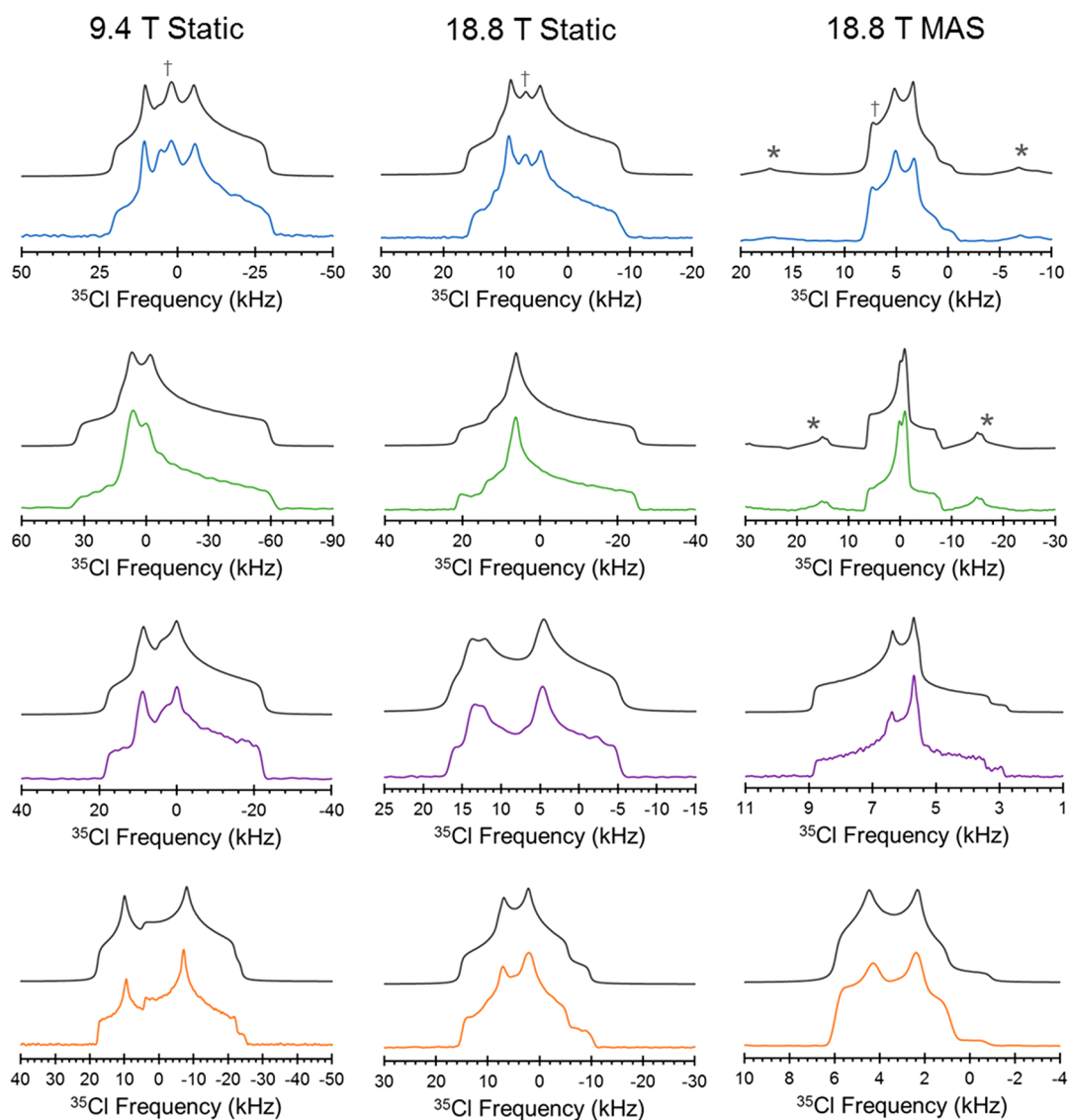


Figure 2. Experimental $^{35}\text{Cl}\{^1\text{H}\}$ SSNMR spectra of L-tyrosine methyl ester HCl (blue), glycine ethyl ester HCl (green), guanidine HCl (purple), L-ornithine HCl (orange), and corresponding analytical simulations (gray). Spectra of static samples were acquired at 9.4 and 18.8 T and under MAS conditions at 18.8 T. Spinning side bands are marked by asterisks (*). Impurities are marked by a dagger (†).

Revolution 5.0 mm HX static probe with samples packed into 5.0 mm o.d. glass tubes sealed with Teflon tape. All data at a field strength of 18.8 T were obtained at the National High Magnetic Field Laboratory (Tallahassee, Florida) using a Bruker NEO console and an Oxford medium bore (63 mm) magnet, with Larmor frequencies of $\nu_0(^1\text{H}) = 799.32$ MHz, $\nu_0(^{14}\text{N}) = 57.80$ MHz, and $\nu_0(^{35}\text{Cl}) = 78.39$ MHz. These spectra were acquired using a home-built 3.2 mm HX MAS probe with samples packed into 3.2 mm o.d. zirconia rotors. A listing of all acquisition parameters is provided in Tables S1–S5. All pulse sequences and recommended calibration parameters and standards for ^{35}Cl and ^{14}N SSNMR are available from the authors upon request.

^{35}Cl SSNMR. DE experiments were performed under static conditions at 9.4 and 18.8 T, and under MAS conditions at 18.8 T. Static spectra at 9.4 T were obtained using either the Hahn-echo sequence with CT-selective $\pi/2$ pulses or the WURST-CPMG sequence,^{73–76} depending on the breadth of the powder pattern.⁷⁷ Spectra at 18.8 T were acquired using Hahn-echo and rotor-synchronized Hahn-echo sequences with

CT-selective $\pi/2$ pulses and MAS frequencies of $\nu_{\text{rot}} = 12\text{--}18$ kHz. A continuous-wave decoupling field of $\nu_2(^1\text{H}) = 35\text{--}50$ kHz was applied during all DE experiments. $^1\text{H}\rightarrow^{35}\text{Cl}\{^1\text{H}\}$ CP experiments were performed under static conditions at 18.8 T. Experimental conditions include an 8.0 ms Hartman-Hahn match at a 50 kHz ramped-amplitude rf field, a continuous wave decoupling field of $\nu_2(^1\text{H}) = 50$ kHz, and a recycle delay of 3.0 s. Chemical shifts were referenced externally to NaCl(s) at $\delta_{\text{iso}}(^{35}\text{Cl}) = 0.0$ ppm.⁷⁸ All ^{35}Cl SSNMR spectra were processed and analyzed using the ssNake v1.1 software package.⁷⁹ For data obtained from WURST-CPMG acquisitions, echoes were coadded in the time domain prior to Fourier transformation. Uncertainties in the quadrupolar and chemical shift tensor parameters were assessed via bidirectional variation of each parameter and visual comparison of experimental and simulated spectra.

^{14}N SSNMR. These spectra were obtained using the WURST-CPMG sequence,^{73–76} in which 50 μs WURST-80 pulses with a maximum amplitude of $\nu_1(^{14}\text{N}) = 50$ kHz were swept linearly from low to high frequency covering a total

Table 1. Experimental and Calculated ^{35}Cl EFG and Chemical Shift Tensor Parameters for Nutraceuticals^{a,b,c,d,e}

material		C_Q (MHz)	η_Q	δ_{iso} (ppm)	$\Delta\delta$ (ppm)	η_{CSA}	α (deg)	β (deg)	γ (deg)
Systems with One Short Contact									
betaine HCl	exp.	5.95(8)	0.10(2)	95(3)	-40(20)	<i>f</i>	<i>f</i>	0(30)	<i>f</i>
	RPBE-D2*	-5.50	0.15	109	-47	0.35	179	8	170
	XRD	-1.92	0.53	60	35	0.35	152	13	154
Systems with Two Short Contacts									
<i>N,N</i> -dimethylglycine HCl	exp.	4.74(6)	0.74(2)	103(5)	-30(10)	1.0(3)	0(30)	90(30)	0(20)
	RPBE-D2*	4.85	0.74	103	-39	0.19	7	83	61
	XRD	-3.46	0.55	54	-26	0.68	47	21	204
yohimbine HCl	exp.	4.67(6)	0.77(2)	105(5)	-30(10)	1.0(5)	90(40)	65(10)	90(40)
	RPBE-D2*	4.64	0.59	110	69	0.38	104	71	174
	XRD								
Systems without Short Contacts									
α -D-glucosamine HCl	exp.	2.30(5)	0.74(2)	84(3)	30(5)	0.5(2)	15(10)	40(5)	35(5)
	RPBE-D2*	2.50	0.44	89	-59	0.37	59	67	28
	XRD	-2.46	0.61	45	-51	0.29	73	27	35
<i>L</i> -tyrosine methyl ester HCl	exp.	3.18(8)	0.53(2)	101(6)	40(10)	1.0(5)	90(10)	90(10)	90(50)
	RPBE-D2*	3.62	0.67	105	67	0.41	81	85	0
	XRD	2.13	0.82	70	54	0.33	66	87	2
glycine ethyl ester HCl	exp.	3.98(6)	0.87(3)	72(4)	40(5)	0.5(3)	0(50)	0(10)	0(50)
	RPBE-D2*	-4.27	0.92	94	87	0.41	19	5	72
	XRD	3.12	0.90	68	70	0.50	277	90	173
guanidine HCl	exp.	2.65(8)	0.78(4)	101(4)	-50(10)	0.7(2)	0(10)	0(10)	20(10)
	RPBE-D2*	-3.24	0.74	119	-83	0.71	80	2	2
	XRD	-2.21	0.79	68	-61	0.83	168	7	107
<i>L</i> -ornithine HCl	exp.	2.99(6)	0.36(4)	72(3)	-50(10)	0.0(3)	<i>f</i>	70(5)	90(20)
	RPBE-D2*	3.02	0.40	82	-78	0.74	79	62	46
	XRD	3.23	0.28	99	-81	0.69	77	62	45

^aTheoretical EFG and CS tensor parameters were obtained from calculations on XRD-derived structures and structures refined at the RPBE-D2* level. ^bThe experimental uncertainties in the last digit for each value are indicated in parentheses. ^cThe quadrupolar coupling constant and asymmetry parameter are given by $C_Q = eQV_{33}/h$, and $\eta_Q = (V_{11} - V_{22})/V_{33}$. The sign of C_Q cannot be determined from the experimental ^{35}Cl spectra. The principal components of the EFG tensors are ranked $|V_{33}| \geq |V_{22}| \geq |V_{11}|$. ^dThe chemical shift tensors are defined using Haebleren's convention, in which the principal components are ordered $|\delta_{xx} - \delta_{\text{iso}}| \geq |\delta_{yy} - \delta_{\text{iso}}| \geq |\delta_{zz} - \delta_{\text{iso}}|$. The isotropic chemical shift, anisotropy, and asymmetry parameter are given by $\delta_{\text{iso}} = (\delta_{xx} + \delta_{yy} + \delta_{zz})/3$, $\Delta\delta = \delta_{zz} - (\delta_{xx} + \delta_{yy})/2$, and $\eta_{\text{CSA}} = (\delta_{yy} - \delta_{xx})/(\delta_{zz} - \delta_{\text{iso}})$, respectively. ^eThe Euler angles α , β , and γ define the relative orientation of the CS and EFG tensors, as defined by Adiga et al. (see ref 84). ^fThis parameter has little-or-no discernible effect on the appearance of simulated powder patterns.

sweep width of 1.0 MHz (sweep rate of 20 MHz/ms). A continuous-wave decoupling field of $\nu_2(^1\text{H}) = 50$ kHz was applied for the duration of each scan. Individual subspectra were collected at evenly spaced transmitter frequencies at an integer multiple of the spikelet separation (ca. 100 kHz).^{80,81} Only the high-frequency sides of the ^{14}N powder patterns were collected; the low-frequency sides of the patterns were produced by reflection, largely for aesthetic purposes.⁵⁰ ^{14}N SSNMR powder patterns were simulated using the WSOLIDS program.⁸² All ^{14}N chemical shifts were referenced externally to NH_4Cl at $\delta_{\text{iso}}(^{14}\text{N}) = 0.0$ ppm, although these values are not reported due to their inherent uncertainties.

2.4. Density Functional Theory Calculations. All calculations were performed within the framework of plane-wave DFT as implemented in the CASTEP module of BIOVIA Materials Studio 2020. These calculations were conducted on structural models determined from previous X-ray diffraction studies.^{64–71} All calculations used the RPBE functional,⁸³ a plane-wave cutoff energy of 800 eV, a k -point spacing of 0.05 \AA^{-1} , ZORA scalar-relativistic pseudopotentials generated on the fly, and an SCF convergence threshold of 5×10^{-7} eV. Grimme's two-body semiempirical dispersion correction force field (D2; $s_6 = 1$, $d = 20$),⁸⁴ or a modification developed in our laboratory (D2*; $s_6 = 1$, $d = 3.5$)^{60–63} was used where indicated. All structural refinements employed the low-memory

BFGS algorithm,⁸⁵ in which the thresholds for structural convergence include a maximum change in energy of 5×10^{-6} eV atom⁻¹, a maximum displacement of 5×10^{-4} \AA atom⁻¹, and a maximum Cartesian force of 10^{-2} eV \AA^{-1} . Magnetic shielding tensors were calculated using the GIPAW method.⁸⁶ Chlorine magnetic shielding values were converted to the chemical shift scale relative to NaCl(s) at $\delta_{\text{iso}}(^{35}\text{Cl}) = 0$ ppm by setting the calculated magnetic shielding of NH_4Cl to $\delta_{\text{iso}}(^{35}\text{Cl}) = 120$ ppm. Euler angles specifying the relative orientation of the chemical shift and EFG tensors were extracted from the CASTEP output files using the program EFGShield 4.1.⁸⁷ The agreement between calculated and experimental ^{35}Cl EFG tensor parameters is quantified by the RMS EFG distance, Γ_{RMS} , as discussed in previous work (Supporting Information).⁶²

3. RESULTS AND DISCUSSION

3.1. ^{35}Cl SSNMR and DFT Studies of Bulk Phases of Nutraceuticals. $^{35}\text{Cl}\{^1\text{H}\}$ SSNMR CT powder patterns were acquired for eight nutraceuticals (Figures 1–2). The spectra were obtained at 9.4 T under static conditions, as well as at 18.8 T under both static and MAS conditions. Since the manifestations of the SOQI and CSA in CT patterns have distinct dependences on the strength of the magnetic field (i.e., broadening resulting from these interactions scale proportional

Table 2. H \cdots Cl $^-$ Contacts and ^{35}Cl SSNMR Parameters for Nutraceuticals, as Calculated for Structures Refined at the RPBE-D2* Level

material	contact type ^a	H \cdots Cl $^-$ distance ^b (Å)	X \cdots Cl $^-$ distance ^c (Å)	X-H \cdots Cl $^-$ angle ^d (deg)	C _Q (MHz)	η_Q	δ_{iso} (ppm)
Systems with One Short Contact							
betaine HCl	ROOH \cdots Cl $^-$	2.008	2.962	170.6	-5.50	0.15	109
Systems with Two Short Contacts							
<i>N,N</i> -dimethylglycine HCl	ROOH \cdots Cl $^-$	2.073	3.013	168.2	4.85	0.74	103
	R ₃ NH $^+$ \cdots Cl $^-$	2.135	3.102	165.4			
Yohimbine HCl	R ₃ NH $^+$ \cdots Cl $^-$	2.109	3.103	176.2	4.64	0.59	110
	R ₂ NH \cdots Cl $^-$	2.251	3.216	174.3			
Systems without Short Contacts							
α -D-glucosamine HCl	ROH \cdots Cl $^-$	2.210	3.130	167.8	2.50	0.44	89
	ROH \cdots Cl $^-$	2.216	3.148	176.0			
	ROH \cdots Cl $^-$	2.258	3.175	167.1			
	RNH ₃ $^+$ \cdots Cl $^-$	2.291	3.187	151.9			
<i>L</i> -tyrosine methyl ester HCl	RNH ₃ $^+$ \cdots Cl $^-$	2.131	3.102	168.0	3.62	0.67	105
	RNH ₃ $^+$ \cdots Cl $^-$	2.186	3.156	168.4			
	ROH \cdots Cl $^-$	2.200	3.128	172.9			
	RNH ₃ $^+$ \cdots Cl $^-$	2.344	3.225	149.8			
glycine ethyl ester HCl	RNH ₃ $^+$ \cdots Cl $^-$	2.221	3.185	166.3	-4.27	0.92	94
	RNH ₃ $^+$ \cdots Cl $^-$	2.323	3.174	145.2			
	RNH ₃ $^+$ \cdots Cl $^-$	2.332	3.228	151.8			
guanidine HCl	C(NH ₂) ₃ $^+$ \cdots Cl $^-$	2.326, 2.468	3.724	155.8, 148.2	-3.24	0.74	119
	C(NH ₂) ₃ $^+$ \cdots Cl $^-$	2.333, 2.488	3.739	155.6, 149.1			
	C(NH ₂) ₃ $^+$ \cdots Cl $^-$	2.336, 2.418	3.707	154.5, 150.6			
<i>L</i> -ornithine HCl	RNH ₃ $^+$ \cdots Cl $^-$	2.209	3.147	159.2	3.02	0.40	82
	RNH ₃ $^+$ \cdots Cl $^-$	2.313	3.206	151.5			
	RNH ₃ $^+$ \cdots Cl $^-$	2.330	3.240	154.7			

^aIndicates the functional group involved in the H \cdots Cl $^-$ bond (e.g., RNH₃ $^+$ \cdots Cl $^-$ and R₃NH $^+$ \cdots Cl $^-$ signify positively charged primary and tertiary ammonium type hydrogen contacts, respectively, R₂NH \cdots Cl $^-$ signifies a secondary ammonium contact, C(NH₂)₃ $^+$ \cdots Cl $^-$ signifies a guanidinium contact, ROOH \cdots Cl $^-$ signifies a carboxylic acid contact, and ROH \cdots Cl $^-$ signifies an alcohol contact). ^bH \cdots Cl $^-$ hydrogen bonds (<2.6 Å), as determined from crystal structures refined at the RPBE-D2* level. Two distances are listed for contacts with guanidinium ions. ^cX \cdots Cl $^-$ interatomic distances (X = N, O), as determined from crystal structures refined at the RPBE-D2* level. ^dAngle between the hydrogen-bond donor atom (X = N, O), the hydrogen atom, and the chloride anion. Two angles are listed for contacts with guanidinium ions.

to B_0^{-1} and B_0 , respectively), acquisition of spectra at two fields allows accurate determinations of the EFG and chemical shift tensors, as well as the set of Euler angles defining the relative orientation of their principal axis systems (see Table 1 for definitions of all parameters).⁸⁷ Acquisition under MAS conditions with appropriate spinning rates averages the effects of CSA, resulting in powder patterns that are dominated by the effects of a partially averaged SOQI. The WURST-CPMG sequence was used to obtain all spectra in which the pattern breadths were greater than ca. 100 kHz, whereas all other spectra were obtained using Hahn-echo (static) or rotor-synchronized Hahn-echo (MAS) sequences. Each pattern arises from a single chloride anion, consistent with the known crystal structures (i.e., $Z' = 1$). The ^{35}Cl SSNMR spectra for the nutraceuticals were simulated using an eight-parameter fit, as reported in Table 1. The spectra are indicative of samples of high purity, with only the spectra of *L*-tyrosine methyl ester HCl revealing a minor impurity (N.B.: This phase is not apparent in the PXRD pattern, demonstrating the ability of ^{35}Cl SSNMR to detect small quantities of impurities that other analytical techniques cannot).

The ^{35}Cl EFG tensors of chloride ions are strongly influenced by H \cdots Cl $^-$ hydrogen bonds (i.e., H \cdots Cl $^-$ contacts < 2.6 Å,¹⁶ including the types of hydrogen-donating functional groups and their spatial arrangement, Table 2).²⁰ Hydrogen bonds that exert the most influence ^{35}Cl EFG tensors are those in which the H \cdots Cl $^-$ distance is less than ca. 2.2 Å, which we

define here as short contacts.²⁰ When a chloride ion has a single short contact, the largest component of the EFG tensor, V_{33} , is almost always oriented along or near the contact axis, and the resulting ^{35}Cl spectrum is typically characterized by a $C_Q(^{35}\text{Cl})$ of relatively large magnitude and an η_Q close to zero (i.e., an EFG tensor of axial or near-axial symmetry). In contrast, when a chloride environment features three or more short contacts, the magnitudes of $C_Q(^{35}\text{Cl})$ are typically smaller, and the values of η_Q deviate substantially from axial symmetry. DFT calculations consistently predict positive EFGs oriented in the directions of the shortest contacts (though the sign of $C_Q(^{35}\text{Cl})$ cannot be determined directly from the ^{35}Cl SSNMR spectra).²⁰ Chlorine chemical shift tensors do not have simple structural relationships of this nature and are somewhat more challenging to measure accurately when the ^{35}Cl CT patterns are dominated by second-order quadrupolar effects (i.e., uncertainties in CS tensor parameters and Euler angles are large, even from analysis of high-field spectra); thus, we restrict our remaining discussion to ^{35}Cl EFG tensors and their related structural inferences.

Plane-wave DFT calculations are necessary for refining the structures of organic materials and providing relationships between NMR tensor parameters and molecular-level structure. Crystal structures determined from XRD often feature poorly resolved or undetermined hydrogen atom positions, making such structures unreliable for calculations of ^{35}Cl EFG tensors. Furthermore, conventional plane-wave

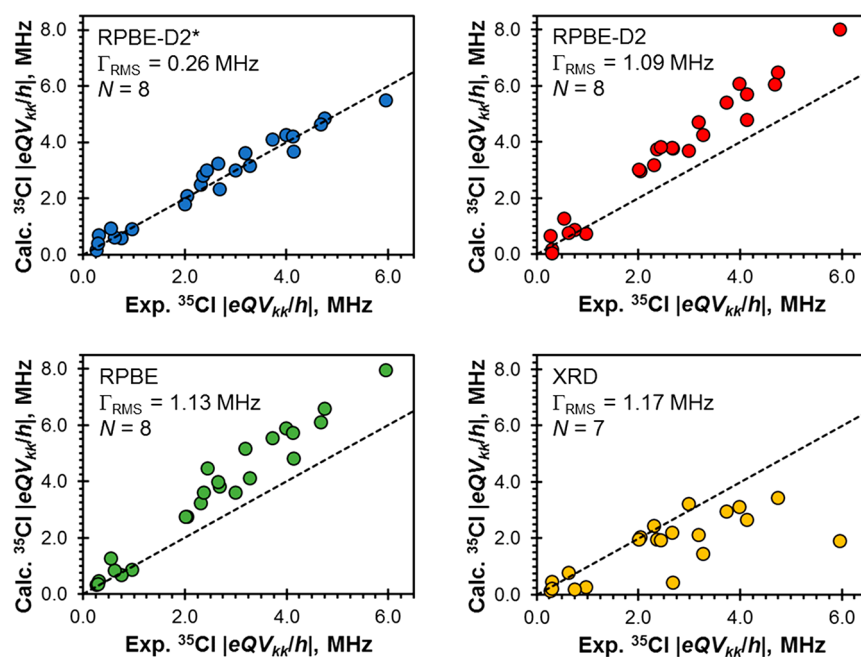


Figure 3. Relationships between experimental and calculated principal components of ^{35}Cl EFG tensors (V_{kk} , where $k = 1, 2, 3$). Calculations of ^{35}Cl EFG tensors were performed on structures that were refined at the RPBE-D2* (blue), RPBE-D2 (red), and RPBE (green) levels or on unrefined structures that were obtained by X-ray diffraction (yellow). The dotted black lines indicate perfect agreement between calculation and experiment. Γ_{RMS} and N denote the root-mean-square EFG distance and the number of chlorine sites, respectively.

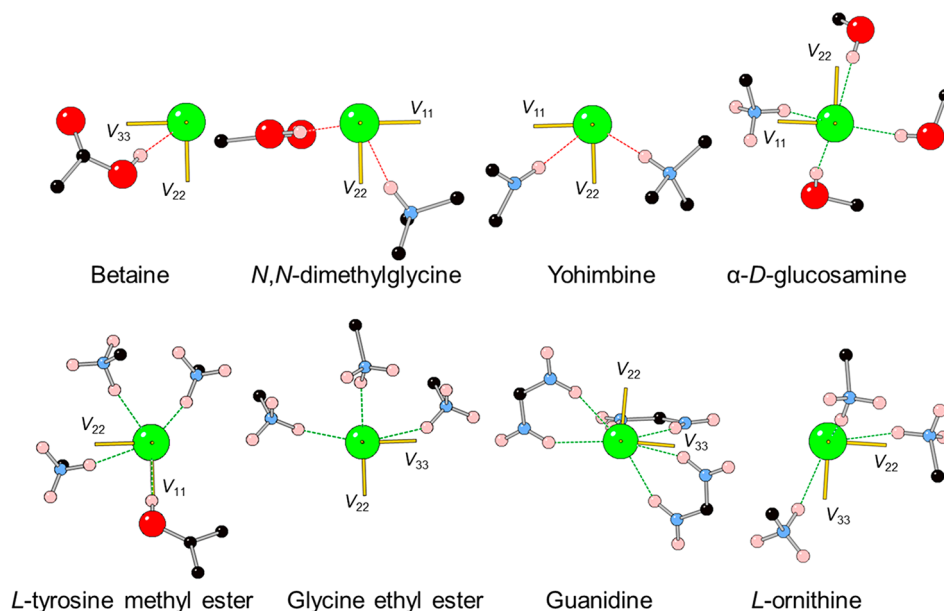


Figure 4. ^{35}Cl EFG tensor orientations for eight nutraceuticals, as calculated for structures refined at the RPBE-D2* level. $\text{H}\cdots\text{Cl}^-$ hydrogen bonds (<2.6 Å) are shown as dotted green lines, whereas short contacts (<2.2 Å) are shown as dotted red lines. The three yellow vectors represent the orientations of the principal components of the EFG tensors (V_{11} , V_{22} , and V_{33}).

DFT structural refinements result in systematic underestimations of $\text{H}\cdots\text{Cl}^-$ bond lengths, leading to overestimations of the magnitudes of the individual principal components of the EFG tensors. To overcome these difficulties, our group has proposed several semiempirical dispersion force field corrections.^{60–63} The model used here, which we denote RPBE-D2*, is based on a reparameterization of the atomic-pairwise force field correction of Grimme,⁸⁴ in which the form of the damping function has been altered such that calculation on the energy minimized structures of organic solids result in accurate

values of EFG tensors. The results obtained using the RPBE-D2* method are compared with those using the RPBE-D2 method (i.e., with Grimme's standard parametrization of the D2 force field), as well as the RPBE method (i.e., without the inclusion of dispersion). A summary of all calculations is provided in Table S6.

For the eight nutraceuticals, plane-wave DFT calculations are presented for models based on structures obtained via SCXRD methods and for models that were refined using the original structures as starting points (Figure 3, Table 1).

Calculations on unrefined XRD-derived structures result in poor agreement with experimental ^{35}Cl EFG tensors, as described by the large value of the EFG distance, $\Gamma_{\text{RMS}}(^{35}\text{Cl}) = 1.17$ MHz. Calculations on structures refined at the RPBE-D2 and RPBE levels result in comparable values of $\Gamma_{\text{RMS}}(^{35}\text{Cl}) = 1.09$ and 1.13 MHz, respectively. In contrast, calculations on structures that were refined at the RPBE-D2* level result in excellent agreement with the experiment, as described by the comparatively small value of $\Gamma_{\text{RMS}}(^{35}\text{Cl}) = 0.26$ MHz.

Because the model structures obtained from RPBE-D2* calculations result in reliable predictions of ^{35}Cl EFG tensors, it is possible to assess the relationships between $\text{H}\cdots\text{Cl}^-$ hydrogen bonding environments and ^{35}Cl EFG tensor parameters and orientations (Table 2, Figure 4), in order to see if they hold consistent with those from previous studies,^{19,20} and for potential future use in NMR crystallographic applications. Some general observations are made in the discussion that follows.

Systems with One Short Contact. The chloride ion environment in betaine HCl features a single short contact with a ROOH group, with the shortest $\text{H}\cdots\text{Cl}^-$ distance of any of the compounds herein (2.008 Å), as well as the value of $C_{\text{Q}}(^{35}\text{Cl})$ with the greatest magnitude (5.95 MHz). The largest principal component, V_{33} , is oriented in the general direction of the $\text{H}\cdots\text{Cl}^-$ contact axis, which is consistent with the low value of η_{Q} (i.e., approaching 0, indicating an EFG tensor approaching axial symmetry). DFT calculations demonstrate that the sign of $C_{\text{Q}}(^{35}\text{Cl})$ is negative (i.e., the EFGs are positive along the axis of the short contact, since $Q(^{35}\text{Cl}) = -8.165$ fm²).⁸⁸

Systems with Two Short Contacts. The Cl^- ion environments in *N,N*-dimethylglycine HCl and yohimbine HCl feature two short contacts with various types of hydrogen-bond donating moieties. DFT calculations show that the signs of $C_{\text{Q}}(^{35}\text{Cl})$ are positive and that V_{33} is oriented approximately perpendicular to the $\text{H}\cdots\text{Cl}^- \cdots \text{H}$ plane formed by the two short contacts in each case, which is consistent with positive EFGs in the $\text{H}\cdots\text{Cl}^- \cdots \text{H}$ plane, and negative EFGs perpendicular to this plane. Since V_{11} and V_{22} are in this plane, they must have different magnitudes, consistent with high values of η_{Q} (i.e., approaching 1) that describe highly nonaxially symmetric EFG tensors.

Systems without Short Contacts. Each of these five systems (Table 2) feature multiple hydrogen bonds that are all greater than ca. 2.2 Å, and unlike the cases above, the orientations of the EFG tensors are less constrained by symmetry or pseudosymmetry elements and vary from system to system. The local environments in α -D-glucosamine HCl and L-tyrosine methyl ester HCl feature multiple hydrogen bonds with alcohol and amine moieties. Similar to the two-contact systems, DFT calculations show that the sign of $C_{\text{Q}}(^{35}\text{Cl})$ is positive, with V_{33} oriented approximately perpendicular to the $\text{H}\cdots\text{Cl}^- \cdots \text{H}$ plane formed by the two shortest hydrogen bonds (which is consistent with the midrange values of η_{Q}). In contrast, the chloride ion environments in glycine ethyl ester HCl, guanidine HCl, and L-ornithine HCl involve only nitrogen-containing moieties. For glycine ethyl ester HCl and guanidine HCl, DFT calculations show that the sign of $C_{\text{Q}}(^{35}\text{Cl})$ is negative and that V_{33} resides approximately within the $\text{H}\cdots\text{Cl}^- \cdots \text{H}$ plane formed by the two shortest hydrogen bonds. In L-ornithine HCl, the chloride ion features three hydrogen bonds involving RNH_3^+ groups. DFT

calculations demonstrate that the sign of $C_{\text{Q}}(^{35}\text{Cl})$ is positive, with V_{22} oriented along the shortest hydrogen bonding axis.

To summarize, these observations are consistent with those from our previous studies of anhydrous HCl salts,²⁰ and demonstrate that it is possible to make a preliminary qualitative assessment of Cl^- environments in the absence of crystallographic structural data. When a chloride environment features a single short contact, the sign of $C_{\text{Q}}(^{35}\text{Cl})$ is negative, and the positive principal component V_{33} is oriented along or near the axis of the short contact. For chloride environments that feature two contacts in a nonlinear spatial arrangement, the sign of $C_{\text{Q}}(^{35}\text{Cl})$ is positive, and the negative principal component V_{33} is oriented approximately perpendicular to the $\text{H}\cdots\text{Cl}^- \cdots \text{H}$ plane formed by the two short contacts, whereas the EFGs are positive in the directions of the two short contacts. Systems that do not feature short contacts do not have any apparent trends that are consistent between all chloride ions; however, for each system considered in this study, the EFGs are positive in the direction of one of the hydrogen bonds or within a plane formed by two hydrogen bonds. Again, it is anticipated that this growing data set of relationships between ^{35}Cl EFG tensors (parameters and orientations) and chloride ion hydrogen-bonding environments will underpin rapid NMR crystallographic assessments of structure, not only in bulk samples but also in dosage forms.

3.2. ^{35}Cl SSNMR Study of a Dosage Form of α -D-Glucosamine HCl. Dosage forms of APIs and nutraceuticals often consist of micro- or nanocrystalline domains of the active ingredient dispersed in a complex matrix of excipients. The presence of excipient molecules can inhibit molecular-level characterization of the active ingredients in dosage forms using conventional analysis techniques such as PXRD, thermal analysis, water sorption analysis, and vibrational spectroscopy, especially when the wt % of the active ingredient is low. Simple one-dimensional ^1H and ^{13}C SSNMR spectroscopic techniques are often hampered due to interfering signals arising from the excipient molecules. However, ^{35}Cl SSNMR spectroscopy can be used to analyze dosage forms because excipients generally do not contain chloride ions; thus, it is an ideal technique for phase identification, structural characterization, and quantification of nutraceuticals in dosage forms.²³

To demonstrate the utility of ^{35}Cl SSNMR for probing dosage forms of nutraceuticals, we have selected a dosage form containing the active ingredient α -D-glucosamine HCl (1500 mg), as well as methylsulfonylmethane (1500 mg), hyaluronic acid (3.3 mg), and an unspecified quantity of excipients (i.e., a maximum of 50 wt % α -D-glucosamine HCl). $^{35}\text{Cl}\{^1\text{H}\}$ DE and $^1\text{H}\rightarrow^{35}\text{Cl}\{^1\text{H}\}$ CP experiments were used to analyze a bulk sample of α -D-glucosamine HCl and the dosage form (Figure 5, Table 3). Ideal CP conditions (including the Hartmann–Hahn matching conditions, contact time, recycle delay) were determined for the bulk phase and applied without change to the dosage form (this allows for quantification of all of the nutraceutical in microcrystalline form, *vide infra*). The $^{35}\text{Cl}\{^1\text{H}\}$ DE experiments were acquired with 2048 scans and a recycle delay of 2.0 s, resulting in a total experiment time of ca. 70 min. In contrast, the CP experiments were acquired with 512 scans and a 3.0 s recycle delay, resulting in a total experiment time of ca. 26 min. The CP spectra of the bulk and dosage forms feature higher S/N ratios and sharper spectral features than those of the $^{35}\text{Cl}\{^1\text{H}\}$ DE spectra, demonstrating the utility of CP techniques for the study of dosage forms

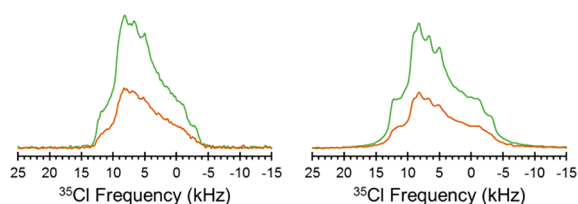


Figure 5. A comparison of static ^{35}Cl SSNMR spectra (18.8 T) of a bulk form (green) and a dosage form (orange) of α -D-glucosamine HCl. The spectra were obtained using either a Hahn-echo sequence (left) or a $^1\text{H}\rightarrow^{35}\text{Cl}$ cross-polarization sequence. Additional active ingredients in the dosage form include methylsulfonylmethane and hyaluronic acid, which do not contain chloride ions.

Table 3. Acquisition Parameters and Results of wt % Quantification Using $^{35}\text{Cl}\{^1\text{H}\}$ Direct Excitation and $^1\text{H}\rightarrow^{35}\text{Cl}\{^1\text{H}\}$ Cross-Polarization Methods for Bulk and Dosage Forms of α -D-Glucosamine HCl

	$^{35}\text{Cl}\{^1\text{H}\}$ direct excitation		$^1\text{H}\rightarrow^{35}\text{Cl}\{^1\text{H}\}$ Cross-Polarization	
	bulk	dosage	bulk	dosage
sample mass (mg)	65.0	75.8	65.0	75.8
wt scaling factor ^a	1.00	0.86	1.00	0.86
no. of scans	2048	2048	512	512
relaxation delay (s)	2.0	2.0	3.0	3.0
experimental time (min)	70	70	26	26
wt % nutraceutical ^b	100	44	100	43

^aThe wt scaling factor accounts for the different sample masses. ^bThe wt % nutraceutical in the bulk form was assumed to be 100% because no impurity phases were detected through PXRD or ^{35}Cl SSNMR spectroscopy.

(again, this is particularly useful if the wt % of the active ingredient is low).

The $^{35}\text{Cl}\{^1\text{H}\}$ DE and $^1\text{H}\rightarrow^{35}\text{Cl}\{^1\text{H}\}$ CP spectra indicate that the dosage form contains the same phase of α -D-glucosamine HCl as the bulk form, as indicated by the positions of key discontinuities in the patterns. The spectra of the dosage form do not show any additional features that may arise from interfering signals from the excipients or additional active ingredients (e.g., in cases of disproportionation or uptake of water under ambient conditions, sharp/narrow patterns are often observed overlapping with the much broader CT patterns arising from the HCl salt of the active ingredient).²³ In addition, the relative integrated signal intensities of the patterns in the ^{35}Cl NMR spectra of the bulk and dosage forms can be used to quantify the content of nutraceutical in the latter (for both DE and CP experiments, after scaling the signal intensities by the relative mass of sample). From the $^{35}\text{Cl}\{^1\text{H}\}$ DE spectra, this ratio suggests that the dosage form consists of 44% α -D-glucosamine HCl, whereas the CP spectra suggest 43%. Both values are consistent with the stated amount of the active ingredient in the dosage form (*vide supra*), demonstrating that $^{35}\text{Cl}\{^1\text{H}\}$ DE and CP methods are useful for phase identification and quantification of dosage forms of nutraceuticals.

Finally, we make several comments regarding the general applicability of ^{35}Cl SSNMR spectroscopy to the study of nutraceuticals in dosage forms, some of which have been considered in more detail in previous work from our laboratory.²³ (i) for the acquisition of wide-line and/or UW patterns, the WURST-CPMG or BRAIN-CP sequences (or

even sequences and pulse sequences designed using optimal control theory) may provide avenues for more uniform excitation and/or refocusing of spin polarization, resulting in undistorted and uniformly excited patterns;^{59,89–92} (ii) if multiple chlorine sites are present (whether corresponding to multiple chlorine sites in the same crystal lattice, two distinct nutraceutical phases within the same formulation, or some physical mixture of dosage forms), one must account for differences in the relaxation rates T_1 and T_2^{eff} and/or optimal CP conditions for calibrating experiments — in such situations, one can use relaxation-assisted separation techniques to obtain spectra corresponding to individual chlorine sites;^{93,94} (iii) the additional signal enhancement afforded by dynamic nuclear polarization^{22,44} and/or ^1H -detected ultrafast MAS methods^{40–43} could allow similar analyses to be conducted in a shorter period of time, or on dosage forms with much lower wt % of nutraceutical; and (iv) ^{35}Cl SSNMR can be used to assess *in situ* interconversions between solid forms of APIs,²⁴ to detect signals corresponding to the products of disproportionation reactions,²³ and for other quality assurance and counterfeit detection purposes. All of these advances have the potential to expand the applications of ^{35}Cl SSNMR to the study of dosage forms of nutraceuticals.

3.3. ^{14}N SSNMR and DFT Studies of Bulk Phases of Nutraceuticals. The $^{14}\text{N}\{^1\text{H}\}$ WURST-CPMG spectra of glycine ethyl ester HCl, α -D-glucosamine HCl, and L-ornithine HCl were acquired rapidly due to short values of $T_1(^{14}\text{N})$ and long values of $T_2^{\text{eff}}(^{14}\text{N})$ (Figure 6). In each case, only the

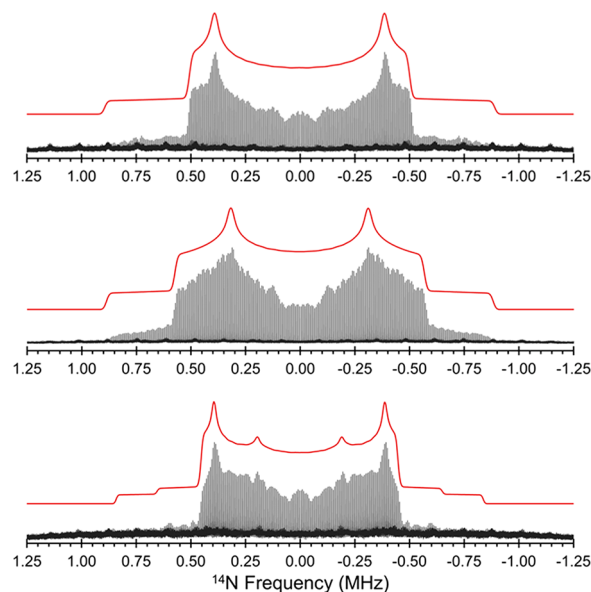


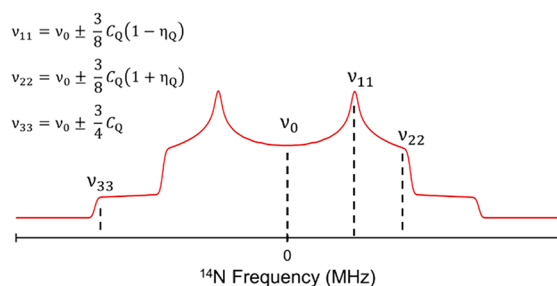
Figure 6. $^{14}\text{N}\{^1\text{H}\}$ WURST-CPMG spectra (18.8 T) of glycine ethyl ester HCl (top), α -D-glucosamine HCl (middle), and L-ornithine HCl. Corresponding analytical simulations are shown in red.

positive frequency sides of the patterns were acquired; the negative frequency sides were generated by mirroring the patterns about the Larmor frequency, largely for aesthetic purposes (N.B.: the effects of nitrogen CSA on these spectra are very small, due to the dominant manifestation of the FOQI).⁵⁰ The positive frequency sides of the patterns were acquired by stepping the transmitter in intervals of ca. 100 kHz in order to achieve uniform patterns. The individual subspectra were obtained in less than nine minutes for glycine ethyl ester

HCl and α -D-glucosamine HCl and in less than five minutes for L-ornithine HCl. Each of the spectra results from eight individual subspectra that were coadded in the frequency domain. The ^{14}N spectrum of L-ornithine HCl is characterized by two overlapping patterns corresponding to the two chemically distinct nitrogen atoms in the molecular structure. In such spectra of integer spin nuclides with low S/N, one must be cautious in the assignment of such discontinuities since artifacts can result from the WURST pulses and the processing of frequency-stepped spectra. The presence of the pattern corresponding to the inner sets of “horns” is more pronounced in individual subspectra acquired with transmitter offsets near ca. 500 kHz, whereas the outer set of “horns” is more pronounced in subspectra with larger transmitter offsets (Figure S2). In all cases, the outer “foot” regions of the Pake-like doublets are the most challenging to detect because of their low intensity; fortunately, this does not impact accurate measurement of the ^{14}N quadrupolar parameters (*vide infra*).

Because of the high degree of symmetry evident in ^{14}N Pake-like powder patterns, the principal components of the ^{14}N EFG tensors can be determined completely by resolving the positions of two key discontinuities in the powder pattern (Scheme 2).⁵⁰ This is most readily accomplished by

Scheme 2. An Idealized ^{14}N Powder Pattern Dominated by the First-Order Quadrupolar Interaction^a



^aThe Pake-like doublet shape results from two overlapping powder patterns arising from the fundamental $0 \leftrightarrow -1$ and $+1 \leftrightarrow 0$ transitions. The relationship between the “horn” (ν_{11}), “shoulder” (ν_{22}), and “foot” (ν_{33}) discontinuities and the EFG tensor parameters C_Q and η_Q are illustrated for the $0 \leftrightarrow -1$ transition.

determining the positions of the “horn” and “shoulder” discontinuities (i.e., ν_{11} and ν_{22} , respectively) since these are located in the highest signal intensity regions of the patterns (the “foot” discontinuities (ν_{33}) are often difficult to resolve due to low S/N, *vide supra*). In practice, the complete powder pattern, or even half of the pattern, does not need to be acquired to fully determine the ^{14}N EFG tensor.⁵⁰ For example, the two key discontinuities in the spectrum of α -D-glucosamine HCl are resolved through judicious placement of the transmitter at a frequency that allows the acquisition of this subspectrum in a single experiment (Figure 7). This targeted acquisition protocol greatly reduces the total experimental time (in the case of α -D-glucosamine HCl, a single subspectrum was acquired in ca. 8.5 min, whereas the complete positive frequency side of the pattern required ca. 68 min to acquire), and potentially allows for the acquisition of ^{14}N NMR spectra in cases of low wt %, large values of $C_Q(^{14}\text{N})$, and/or inconvenient relaxation characteristics.

The $^{14}\text{N}\{^1\text{H}\}$ WURST-CPMG spectra of betaine HCl, L-tyrosine methyl ester HCl, and *N,N*-dimethylglycine HCl were

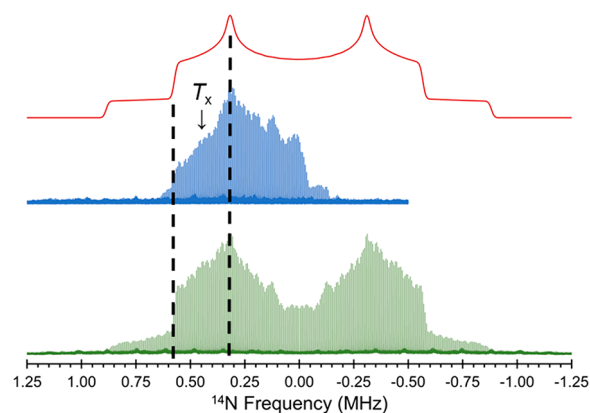


Figure 7. $^{14}\text{N}\{^1\text{H}\}$ WURST-CPMG spectra (18.8 T) of α -D-glucosamine HCl. The complete powder pattern (green) was obtained as a series of eight subspectra by stepping the transmitter frequency in intervals of ca. 100 kHz across the positive frequency half of the pattern; the negative frequency half of the pattern was obtained by mirroring the spectrum about the Larmor frequency. The spectrum in blue was obtained with a single transmitter offset frequency (T_x). The frequencies of the “horn” ($\nu_{11} = 310$ kHz) and “shoulder” ($\nu_{22} = 575$ kHz) discontinuities are marked on the spectrum, from which one can obtain values of C_Q and η_Q by analyzing either the green or blue patterns. The corresponding analytical simulation is shown in red.

obtained as targeted acquisitions of a single subspectrum or “piece” of the entire Pake-like doublet (Figure 8), since the

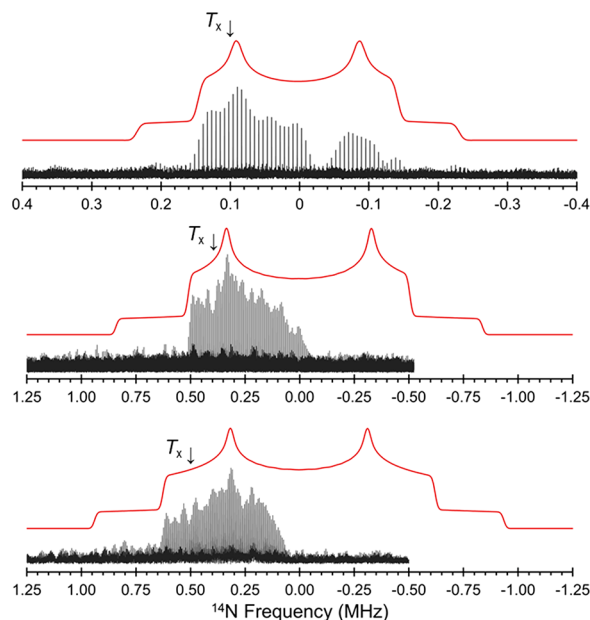


Figure 8. $^{14}\text{N}\{^1\text{H}\}$ WURST-CPMG spectra (18.8 T) of betaine HCl (top), L-tyrosine methyl ester HCl (middle), and *N,N*-dimethylglycine HCl. All spectra were acquired as a single piece with the transmitter frequency indicated (T_x). Corresponding analytical simulations are shown in red.

short values of $T_2^{\text{eff}}(^{14}\text{N})$, and/or long values of $T_1(^{14}\text{N})$ rendered acquisition of the entire patterns impractical. For betaine HCl and L-tyrosine methyl ester HCl, a single piece of the powder pattern was acquired in ca. 17 min. In contrast, the spectrum of *N,N*-dimethylglycine HCl required ca. 15 h to acquire.

Table 4. Experimental and Calculated ^{14}N EFG Tensor Parameters for Nutraceuticals^{a,b,c,d,e}

material (N Site)	coordination	experimental		XRD structures		RPBE-D2* structures	
		C_Q (MHz)	η_Q	C_Q (MHz)	η_Q	C_Q (MHz)	η_Q
glycine ethyl ester HCl	R-NH ₃ ⁺	1.19(1)	0.13(1)	1.88	0.03	1.41	0.10
L-tyrosine methyl ester HCl	R-NH ₃ ⁺	1.12(1)	0.21(1)	1.66	0.13	1.32	0.21
α -D-glucosamine HCl	R-NH ₃ ⁺	1.18(1)	0.29(1)	1.70	0.15	1.34	0.26
L-ornithine HCl (N1)	R-NH ₃ ⁺	1.12(2)	0.07(2)	1.20	0.13	1.24	0.06
L-ornithine HCl (N2)	R-NH ₃ ⁺	0.87(2)	0.41(2)	0.89	0.44	1.02	0.27
N,N-dimethylglycine HCl	R-NH(CH ₃) ₂ ⁺	1.25(1)	0.33(1)	-1.91	0.24	-1.46	0.30
betaine HCl	R-N(CH ₃) ₃ ⁺	0.31(2)	0.24(3)	0.38	0.16	0.34	0.08
guanidine HCl (N1)	R-NH ₂	3.4507	0.430	-3.07	0.94	-3.54	0.47
guanidine HCl (N2)	R-NH ₂	3.4683	0.421	-3.10	0.88	-3.55	0.46
guanidine HCl (N3)	R = NH ₂ ⁺	3.5811	0.385	-3.14	0.86	-3.69	0.42
yohimbine HCl (N1)	R ₂ -NH					-2.80	0.46
yohimbine HCl (N2)	R ₃ -NH ⁺					-1.37	0.15

^aTheoretical EFG tensor parameters were obtained from calculations on XRD-derived structures and structures refined at the RPBE-D2* level.

^bThe experimental uncertainties in the last digit for each value are indicated in parentheses. ^cThe quadrupolar coupling constant and asymmetry parameter are given by $C_Q = eQV_{33}/h$, and $\eta_Q = (V_{11} - V_{22})/V_{33}$. The sign of C_Q cannot be determined from the experimental ^{14}N spectra. The principal components of the EFG tensors are ranked $|V_{33}| \geq |V_{22}| \geq |V_{11}|$. ^dThe experimental values for guanidine HCl are from an NQR spectroscopy study by Chen and Dodgen (see ref 94). All other experimental values are from this work. ^eExperimental values were determined at 77 K for guanidine HCl and at room temperature for all other materials.

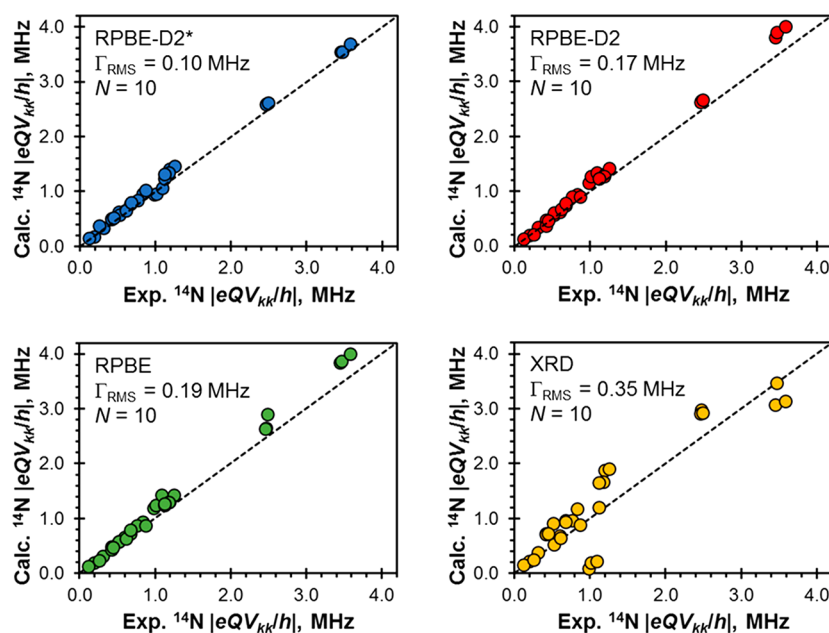


Figure 9. Relationships between experimental and calculated principal components of ^{14}N EFG tensors (V_{kk} where $k = 1, 2, 3$). Calculations of ^{14}N EFG tensors were performed on structures that were refined at the RPBE-D2* (blue), RPBE-D2 (red), and RPBE (green) levels or on unrefined structures that were obtained by X-ray diffraction (yellow). The dotted black lines indicate perfect agreement between calculation and experiment. Γ_{RMS} and N denote the root-mean-square EFG distance and the number of nitrogen sites, respectively.

Unfortunately, we were not able to obtain the ^{14}N spectrum for yohimbine HCl or guanidine HCl using these methods, possibly due to the anticipated breadths of the patterns (cf. Table 4) and/or the potentially short values of $T_2^{\text{eff}}(^{14}\text{N})$. Additional acquisitions using the BRAIN-CP sequence,⁵⁵ or a quadrupolar echo sequence with the transmitter placed at the anticipated positions of the discontinuities of the pattern, did not yield signal in these cases. We note that the broad nitrogen patterns have been observed through indirect ^{14}N - ^1H HMQC experiments.^{95,96} Additionally, guanidine HCl has been studied previously by ^{14}N nuclear quadrupole resonance (NQR) spectroscopy.⁹⁷⁻⁹⁹ A study conducted at room temperature detected only two distinct resonances, indicating an averaging

of the three nitrogen sites due to molecular-level motions,⁹⁹ whereas a different study conducted at 77 K resolved six distinct resonances, corresponding to the three nitrogen atoms in the crystal structure.⁹⁹

We have calculated the ^{14}N EFG tensors for each of the nitrogen sites within the eight nutraceuticals. These calculations were performed on models based on SCXRD structures and refined structural models (Table 4, Figure 9). Calculations of the XRD-derived structures result in poor agreement with experimental ^{14}N EFG tensors, characterized by $\Gamma_{\text{RMS}}(^{14}\text{N}) = 0.35$ MHz. Calculations on structures performed at the RPBE-D2 and RPBE levels result in values of $\Gamma_{\text{RMS}}(^{14}\text{N}) = 0.17$ and 0.19 MHz, respectively, whereas calculations on structures that

were refined at the RPBE-D2* level result in better agreement with the experiment, as described by the lower value of $\Gamma_{\text{RMS}}(^{14}\text{N}) = 0.10$ MHz. We note the following: (i) the values of $C_{\text{Q}}(^{14}\text{N})$ for the pseudotetrahedral nitrogen sites are systematically overestimated for each of the refined structural models; (ii) the ^{14}N EFG tensor parameters of guanidine HCl are most strongly influenced by structural refinement, with calculation on the RPBE-D2* structure leading to the best results; (iii) calculations of ^{35}Cl EFG tensors are generally more sensitive to structural refinements, with only calculations on RPBE-D2* structures resulting in good agreement with experiment (cf. §3.1).

The ^{14}N EFG tensors measured in this study correspond to nitrogen atoms in pseudotetrahedral chemical environments, including RNH_3^+ ($\text{R} \neq \text{CH}_3$), $\text{RN}(\text{CH}_3)_3^+$, $\text{RNH}(\text{CH}_3)_2^+$, and $\text{RR}'\text{R}''\text{NH}^+$ moieties. ^{14}N EFG tensor parameters for the nitrogen sites featuring RNH_3^+ geometries are consistent with previous studies of such moieties;^{51–53} the values of $C_{\text{Q}}(^{14}\text{N})$ range between 0.87 and 1.19 MHz, and DFT calculations suggest that the signs of $C_{\text{Q}}(^{14}\text{N})$ for these sites are positive (i.e., the values of V_{33} are positive, since $Q(^{14}\text{N}) = 2.044 \text{ fm}^2$).⁸⁸ The nitrogen atom in betaine HCl belongs to a $\text{RN}(\text{CH}_3)_3^+$ group and is predicted to have a positive value of $C_{\text{Q}}(^{14}\text{N})$; because the nitrogen atom is covalently bound to four carbon atoms, the local symmetry is nearly tetrahedral, and the value of $C_{\text{Q}}(^{14}\text{N})$ is accordingly small (0.31 MHz). The nitrogen atom in *N,N*-dimethylglycine HCl belongs to a $\text{RNH}(\text{CH}_3)_2^+$ group and consequently has a slightly larger value of $C_{\text{Q}}(^{14}\text{N})$ (1.25 MHz), which DFT calculations indicate to be negative. Similarly, one of the nitrogen sites in yohimbine HCl resides in a pseudotetrahedral $\text{RR}'\text{R}''\text{NH}^+$ environment and is predicted to have a value of $C_{\text{Q}}(^{14}\text{N}) = -1.37$ MHz, which is in agreement with the sign of the calculated value for the same nitrogen-containing moiety in *N,N*-dimethylglycine HCl.

The asymmetry parameters of ^{14}N EFG tensors of pseudotetrahedral nitrogen atoms are influenced by the local hydrogen bonding environments; as such, they may be useful as metrics for assessing the strengths of intermolecular interactions. In the absence of significant hydrogen bonding in pseudotetrahedral RNH_3^+ nitrogen moieties, low values of η_{Q} (i.e., $0.00 \leq \eta_{\text{Q}} \leq 0.30$; $V_{11} \approx V_{22}$) are often observed, since V_{33} is directed along or close to the R–N bond axis. Stronger hydrogen bonding results in small differences in N–H bond lengths, which creates observable differences in the magnitudes of V_{11} and V_{22} , while still having V_{33} oriented along/near the R–N bond axis, resulting in intermediate values of η_{Q} ($0.30 \leq \eta_{\text{Q}} \leq 0.75$).

In contrast with the pseudotetrahedral nitrogen sites, the three nitrogen sites in guanidine HCl and one of the sites in yohimbine HCl reside in pseudoplanar environments and have correspondingly larger values of $C_{\text{Q}}(^{14}\text{N})$ and intermediate values of η_{Q} . The planar site in yohimbine HCl is predicted to have $C_{\text{Q}}(^{14}\text{N}) = -2.80$ MHz, whereas the three sites in guanidine HCl have measured values of $C_{\text{Q}}(^{14}\text{N})$ between -3.54 MHz and -3.69 MHz. The $C_{\text{Q}}(^{14}\text{N})$ values of such environments are generally less affected by hydrogen-bonding interactions and represent the best examples of good agreement between theory and experiment.

Finally, we acquired a $^{14}\text{N}\{^1\text{H}\}$ WURST-CPMG spectrum of the dosage form containing α -D-glucosamine HCl (Figure 10). Similar to the spectra of the bulk phases discussed above, this spectrum was acquired in ca. 8.5 min as a single

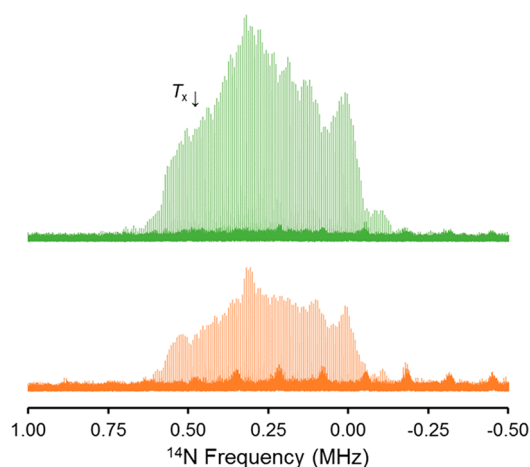


Figure 10. $^{14}\text{N}\{^1\text{H}\}$ WURST-CPMG spectra (18.8 T) of bulk α -D-glucosamine HCl (top) and a dosage form containing the same nutraceutical (bottom). Spectra were acquired as a single piece with the transmitter frequency indicated (T_x).

subspectrum using targeted acquisition with an optimal transmitter frequency suggested by prior analysis of the bulk phase of the nutraceutical. The spectrum demonstrates that the dosage form contains α -D-glucosamine HCl (as indicated by the positions of the “horn” and “shoulder” discontinuities), with no additional features in the pattern arising from nitrogen-containing excipients and/or impurities. Together with the $^{35}\text{Cl}\{^1\text{H}\}$ DE and $^1\text{H} \rightarrow ^{35}\text{Cl}\{^1\text{H}\}$ CP spectra (cf. Figure 5), these results demonstrate that the combination of ^{35}Cl and ^{14}N SSNMR spectroscopy provides a rapid characterization of nutraceutical dosage forms under static conditions. This eliminates the long sample preparation times and costly rotors, caps, and tool kits that are necessary for fast MAS techniques, allowing for the possibility of direct insertion of a powdered nutraceutical or dosage forms (i.e., tablets or capsules) into the probe coil (within a sample container), potentially making these methods suitable for higher-throughput screening of nutraceutical products.

4. CONCLUSIONS

This work has demonstrated that the combination of ^{35}Cl and ^{14}N SSNMR spectroscopic techniques and plane-wave DFT calculations provides important information regarding the molecular-level structures of nutraceuticals. The usefulness of ^{35}Cl SSNMR for the characterization of solid forms of nutraceuticals reflects the fact that ^{35}Cl EFG tensors are strongly influenced by the types and arrangements of the surrounding $\text{H}\cdots\text{Cl}^-$ hydrogen bonds, with even the smallest differences or changes in the local environment influencing the appearances of powder patterns. Additionally, ^{35}Cl SSNMR is useful for rapid fingerprinting, detection of impurities and/or adulterants, identification of potential counterfeited products, and quantification of nutraceuticals in dosage forms. ^{14}N SSNMR spectroscopy provides complementary information to ^{35}Cl SSNMR, especially for cases where the nitrogen atom serves as the donor for $\text{H}\cdots\text{Cl}^-$ hydrogen bonds. Improved experimental methodologies, including those that exploit the inherent symmetry of UW ^{14}N powder patterns using targeted acquisition, allow these spectra to be acquired in minutes for highly receptive samples, suggesting possible usage for the characterization of dosage forms in the future. Finally,

dispersion-corrected plane-wave DFT structural refinements provide better atomic coordinates than is possible through XRD alone, which is necessary for the accurate prediction of EFG tensors from a known crystal structure. Such calculations provide important relationships between NMR parameters and molecular-level structure, which opens the avenue for characterizing novel nutraceutical solid forms in the absence of high-quality diffraction data. Thus, it is hoped that these experimental and computational protocols will serve as a foundation for future NMR crystallographic studies of nutraceuticals in their bulk and dosage forms and may find use in structural prediction algorithms and efforts aiming at detecting impurities in or counterfeit forms of nutraceuticals.

■ ASSOCIATED CONTENT

SI Supporting Information

The Supporting Information is available free of charge at <https://pubs.acs.org/doi/10.1021/acs.molpharmaceut.1c00708>.

SSNMR acquisition parameters, X-ray powder diffractograms, additional ^{14}N SSNMR spectra, and summary of calculated EFG tensor parameters (PDF)

■ AUTHOR INFORMATION

Corresponding Author

Robert W. Schurko – Department of Chemistry & Biochemistry, Florida State University, Tallahassee, Florida 32306, United States; National High Magnetic Field Laboratory, Tallahassee, Florida 32310, United States; orcid.org/0000-0002-5093-400X; Email: rschurko@fsu.edu

Authors

Sean T. Holmes – Department of Chemistry & Biochemistry, Florida State University, Tallahassee, Florida 32306, United States; National High Magnetic Field Laboratory, Tallahassee, Florida 32310, United States

James M. Hook – NMR Facility, Mark Wainwright Analytical Centre, The University of New South Wales, Sydney, New South Wales 2052, Australia; School of Chemistry, The University of New South Wales, Sydney, New South Wales 2052, Australia; orcid.org/0000-0002-1185-7320

Complete contact information is available at: <https://pubs.acs.org/doi/10.1021/acs.molpharmaceut.1c00708>

Notes

The authors declare no competing financial interest.

■ ACKNOWLEDGMENTS

We thank Genentech, The Florida State University, the National High Magnetic Field Laboratory, and the Natural Sciences and Engineering Research Council of Canada (NSERC, RGPIN-2016_06642 Discovery Grant) for funding this research. The National High Magnetic Field Laboratory is supported by the National Science Foundation through NSF/DMR-1644779 and the State of Florida. We also acknowledge the support of the solid-state NMR facilities at the University of Windsor by the Canadian Foundation for Innovation, Ontario Innovation Trust, and the University of Windsor. A portion of this research used resources provided by the X-ray Crystallography Center at the FSU Department of Chemistry

and Biochemistry (FSU075000XRAY). We wish to acknowledge access to NMR spectrometers in the Mark Wainwright Analytical Centre, University of NSW, Sydney, from the Australian Research Council (LE0989541), and to Dr. Aditya Rawal for assistance with acquiring preliminary NMR data.

■ REFERENCES

- (1) Gupta, R. C. *Nutraceuticals: Efficacy, Safety, and Toxicity*; Academic Press: Boston, 2016.
- (2) Mukherjee, P. K.; Harwansh, R. K.; Bahadur, S.; Duraipandiyar, V.; Al-Dhabi, N. A. Factors to Consider in Development of Nutraceutical and Dietary Supplements. In *Pharmacognosy*; Badal, S., Delgoda, R., Eds.; Academic Press: Boston, 2017; pp 653–661.
- (3) Ho, C.-T.; Zheng, Q. Y. *Quality Management of Nutraceuticals*; American Chemical Society: Washington, D.C., 2001.
- (4) *Global Nutraceutical Market Growth Analysis Report, 2020–2027*; Grand View Research, Inc., 2020.
- (5) Dima, C.; Assadpour, E.; Dima, S.; Jafari, S. M. Bioavailability of nutraceuticals: role of the food matrix, processing conditions, the gastrointestinal tract, and nanodelivery systems. *Compr. Rev. Food Sci. Food Saf.* **2020**, *19*, 954–994.
- (6) Klitou, P.; Rosbottom, I.; Simone, E. Synthonic modeling of quercetin and its hydrates: explaining crystallization behavior in terms of molecular conformation and crystal packing. *Cryst. Growth Des.* **2019**, *19*, 4774–4783.
- (7) Klitou, P.; Pask, C. M.; Onoufriadi, L.; Rosbottom, I.; Simone, E. Solid-state characterization and role of solvent molecules on the crystal structure, packing, and physicochemical properties of different quercetin solvates. *Cryst. Growth Des.* **2020**, *20*, 6573–6584.
- (8) Sinha, A. S.; Maguire, A. R.; Lawrence, S. E. Cocrystallization of nutraceuticals. *Cryst. Growth Des.* **2015**, *15*, 984–1009.
- (9) Thipparaboina, R.; Kumar, D.; Chavan, R. B.; Shastri, N. R. Multidrug co-crystals: towards the development of effective therapeutic hybrids. *Drug Discovery Today* **2016**, *21*, 481–490.
- (10) Fulas, O. A.; Laferrrière, A.; Ayoub, G.; Gandrath, D.; Mottillo, C.; Titi, H. M.; Stein, R. S.; Frišči, T.; Coderre, T. J. Drug-nutraceutical co-crystals and salts for making new and improved bi-functional analgesics. *Pharmaceutics* **2020**, *12*, 1144.
- (11) Sarmah, K. K.; Nath, N.; Rao, D. R.; Thakuria, R. Mechanochemical synthesis of drug–drug and drug–nutraceutical multicomponent solids of olanzapine. *CrystEngComm* **2020**, *22*, 1120–1130.
- (12) Thakuria, R.; Sarma, B. Drug–drug and drug–nutraceutical cocrystal/salt as alternative medicine for combination therapy: a crystal engineering approach. *Crystals* **2018**, *8*, 101.
- (13) Wang, L.-Y.; Zhao, M.-Y.; Bu, F.-Z.; Niu, Y.-Y.; Yu, Y.-M.; Li, Y.-T.; Yan, C.-W.; Wu, Z.-Y. Cocrystallization of amantadine hydrochloride with resveratrol: the first drug–nutraceutical cocrystal displaying synergistic antiviral activity. *Cryst. Growth Des.* **2021**, *21*, 2763–2776.
- (14) Sadgrove, N. J. Honest nutraceuticals, cosmetics, therapies, and foods (NCTFs): standardization and safety of natural products. *Crit. Rev. Food Sci. Nutr.* **2021**, 1–16.
- (15) Paulekuhn, G. S.; Dressman, J. B.; Saal, C. Trends in active pharmaceutical ingredient salt selection based on analysis of the orange book database. *J. Med. Chem.* **2007**, *50*, 6665–6672.
- (16) Desiraju, G. R.; Steiner, T. *The Weak Hydrogen Bond in Structural Chemistry and Biology*; Oxford University Press, Inc.: New York, 1999.
- (17) Steiner, T. Hydrogen-bond distances to halide ions in organic and organometallic crystal structures: up-to-date database study. *Acta Crystallogr., Sect. B: Struct. Sci.* **1998**, *54*, 456–463.
- (18) Pindelska, E.; Sokal, A.; Kolodziejski, W. Pharmaceutical cocrystals, salts and polymorphs: advanced characterization techniques. *Adv. Drug Delivery Rev.* **2017**, *117*, 111–146.
- (19) Hamaed, H.; Pawlowski, J. M.; Cooper, B. F. T.; Fu, R.; Eichhorn, S. H.; Schurko, R. W. Application of solid-state ^{35}Cl NMR

to the structural characterization of hydrochloride pharmaceuticals and their polymorphs. *J. Am. Chem. Soc.* **2008**, *130*, 11056–11065.

(20) Hildebrand, M.; Hamaed, H.; Namespetra, A. M.; Donohue, J. M.; Fu, R.; Hung, I.; Gan, Z.; Schurko, R. W. ^{35}Cl solid-state NMR of HCl salts of active pharmaceutical ingredients: structural prediction, spectral fingerprinting and polymorph recognition. *CrystEngComm* **2014**, *16*, 7334–7356.

(21) Namespetra, A. M.; Hirsh, D. A.; Hildebrand, M. P.; Sandre, A. R.; Hamaed, H.; Rawson, J. M.; Schurko, R. W. ^{35}Cl solid-state NMR spectroscopy of HCl pharmaceuticals and their polymorphs in bulk and dosage forms. *CrystEngComm* **2016**, *18*, 6213–6232.

(22) Hirsh, D. A.; Rossini, A. J.; Emsley, L.; Schurko, R. W. ^{35}Cl dynamic nuclear polarization solid-state NMR of active pharmaceutical ingredients. *Phys. Chem. Chem. Phys.* **2016**, *18*, 25893–25904.

(23) Hirsh, D. A.; Su, Y.; Nie, H.; Xu, W.; Stueber, D.; Variankaval, N.; Schurko, R. W. Quantifying disproportionation in pharmaceutical formulations with ^{35}Cl solid-state NMR. *Mol. Pharmaceutics* **2018**, *15*, 4038–4048.

(24) Hirsh, D. A.; Holmes, S. T.; Chakravarty, P.; Peach, A. A.; DiPasquale, A. G.; Nagapudi, K.; Schurko, R. W. *In situ* characterization of waters of hydration in a variable-hydrate active pharmaceutical ingredient using ^{35}Cl solid-state NMR and X-ray diffraction. *Cryst. Growth Des.* **2019**, *19*, 7349–7362.

(25) Peach, A. A.; Hirsh, D. A.; Holmes, S. T.; Schurko, R. W. Mechanochemical syntheses and ^{35}Cl solid-state NMR characterization of fluoxetine HCl cocrystals. *CrystEngComm* **2018**, *20*, 2780–2792.

(26) Vogt, F. G.; Williams, G. R.; Strohmeier, M.; Johnson, M. N.; Copley, R. C. B. Solid-state NMR analysis of a complex crystalline phase of ronacaleret hydrochloride. *J. Phys. Chem. B* **2014**, *118*, 10266–10284.

(27) Vogt, F. G.; Williams, G. R.; Copley, R. C. B. Solid-state NMR analysis of a boron-containing pharmaceutical hydrochloride salt. *J. Pharm. Sci.* **2013**, *102*, 3705–3716.

(28) Iuga, D.; Corlett, E. K.; Brown, S. P. ^{35}Cl - ^1H heteronuclear correlation MAS NMR experiments for probing pharmaceutical salts. *Magn. Reson. Chem.* **2021**, *59*, 1089–1100.

(29) Bryce, D. L.; Gee, M.; Wasylishen, R. E. High-field chlorine NMR spectroscopy of solid organic hydrochloride salts: a sensitive probe of hydrogen bonding environments. *J. Phys. Chem. A* **2001**, *105*, 10413–10421.

(30) Gervais, C.; Dupree, R.; Pike, K. J.; Bonhomme, C.; Profeta, M.; Pickard, C. J.; Mauri, F. Combined first-principles computational and experimental multinuclear solid-state NMR investigation of amino acids. *J. Phys. Chem. A* **2005**, *109*, 6960–6969.

(31) Bryce, D. L.; Sward, G. D. Chlorine-35/37 NMR spectroscopy of solid amino acid hydrochlorides: refinement of hydrogen-bonded proton positions using experiment and theory. *J. Phys. Chem. B* **2006**, *110*, 26461–26470.

(32) Bryce, D. L.; Sward, G. D.; Adiga, S. Solid-state $^{35/37}\text{Cl}$ NMR spectroscopy of hydrochloride salts of amino acids implicated in chloride ion transport channel selectivity: opportunities at 900 MHz. *J. Am. Chem. Soc.* **2006**, *128*, 2121–2134.

(33) Chapman, R. P.; Bryce, D. L. A high-field solid-state $^{35/37}\text{Cl}$ NMR and quantum chemical investigation of the chlorine quadrupolar and chemical shift tensors in amino acid hydrochlorides. *Phys. Chem. Chem. Phys.* **2007**, *9*, 6219–6230.

(34) Chapman, R. P.; Hiscock, J. R.; Gale, P. A.; Bryce, D. L. A solid-state $^{35/37}\text{Cl}$ NMR study of a chloride ion receptor and a GIPAW-DFT study of chlorine NMR interaction tensors in organic hydrochlorides. *Can. J. Chem.* **2011**, *89*, 822–834.

(35) Attrell, R. J.; Widdifield, C. M.; Korobkov, I.; Bryce, D. L. Weak halogen bonding in solid haloanilinium halides probed directly via chlorine-35, bromine-81, and iodine-127 NMR spectroscopy. *Cryst. Growth Des.* **2012**, *12*, 1641–1653.

(36) Socha, O.; Hodgkinson, P.; Widdifield, C. M.; Yates, J. R.; Dracinsky, M. Exploring systematic discrepancies in DFT calculations of chlorine nuclear quadrupole couplings. *J. Phys. Chem. A* **2017**, *121*, 4103.

(37) Penner, G. H.; Webber, R.; O'Dell, L. A. A multinuclear NMR and quantum chemical study of solid trimethylammonium chloride. *Can. J. Chem.* **2011**, *89*, 1036–1046.

(38) Burgess, K. M. N.; Korobkov, I.; Bryce, D. L. A combined solid-state NMR and X-ray crystallography study of the bromide ion environments in triphenylphosphonium bromides. *Chem. - Eur. J.* **2012**, *18*, 5748–5758.

(39) Viger-Gravel, J.; Leclerc, S.; Korobkov, I.; Bryce, D. L. Direct investigation of halogen bonds by solid-state multinuclear magnetic resonance spectroscopy and molecular orbital analysis. *J. Am. Chem. Soc.* **2014**, *136*, 6929–6942.

(40) Pandey, M. K.; Kato, H.; Ishii, Y.; Nishiyama, Y. Two-dimensional proton-detected $^{35}\text{Cl}/^1\text{H}$ correlation solid-state NMR experiment under fast magic angle sample spinning: application to pharmaceutical compounds. *Phys. Chem. Chem. Phys.* **2016**, *18*, 6209–6216.

(41) Wijesekara, A. V.; Venkatesh, A.; Lampkin, B. J.; VanVeller, B.; Lubach, J. W.; Nagapudi, K.; Hung, I.; Gor'kov, P. L.; Gan, Z.; Rossini, A. J. Fast acquisition of proton-detected HETCOR solid-state NMR spectra of quadrupolar nuclei and rapid measurement of NH bond lengths by frequency selective HMQC and RESPDOR pulse sequences. *Chem. - Eur. J.* **2020**, *26*, 7881–7888.

(42) Venkatesh, A.; Hanrahan, M. P.; Rossini, A. J. Proton detection of MAS solid-state NMR spectra of half-integer quadrupolar nuclei. *Solid State Nucl. Magn. Reson.* **2017**, *84*, 171–181.

(43) Venkatesh, A.; Luan, X.; Perras, F. A.; Hung, I.; Huang, W.; Rossini, A. J. t_1 -noise eliminated dipolar heteronuclear multiple-quantum coherence solid-state NMR spectroscopy. *Phys. Chem. Chem. Phys.* **2020**, *22*, 20815–20828.

(44) Zhao, L.; Pinon, A. C.; Emsley, L.; Rossini, A. J. DNP-enhanced solid-state NMR spectroscopy of active pharmaceutical ingredients. *Magn. Reson. Chem.* **2018**, *56*, 583–609.

(45) Vogt, F. G.; Williams, G. R.; Johnson, M. N.; Copley, R. C. B. A spectroscopic and diffractometric study of polymorphism in ethyl 3-[3-(((2R)-3-[[2-(2,3-dihydro-1H-inden-2-yl)-1,1-dimethylethyl]-amino]-2-hydroxypropyl)oxy]-4,5-difluorophenyl)propanoate hydrochloride. *Cryst. Growth Des.* **2013**, *13*, 5353–5367.

(46) Nounou, M. I.; Ko, Y.; Helal, N. A.; Boltz, J. F. Adulteration and counterfeiting of online nutraceutical formulations in the United States: time for intervention? *J. Diet. Suppl.* **2018**, *15*, 789–804.

(47) Buckley, G. J.; Gostin, L. O. *Countering the Problem of Falsified and Substandard Drugs*; National Academic Press: Washington D.C., 2013.

(48) Chandrakumar, N., NMR of Spin-1 Systems in the Solid State. In *NMR Basic Principles and Progress*; Springer-Verlag: Berlin, Heileberg, 1996.

(49) O'Dell, L. A. Direct detection of nitrogen-14 in solid-state NMR spectroscopy. *Prog. Nucl. Magn. Reson. Spectrosc.* **2011**, *59*, 295–318.

(50) Veinberg, S. L.; Lindquist, A. W.; Jaroszewicz, M. J.; Schurko, R. W. Practical considerations for the acquisition of ultra-wideline ^{14}N NMR spectra. *Solid State Nucl. Magn. Reson.* **2017**, *84*, 45–58.

(51) Veinberg, S. L.; Friedl, Z. W.; Harris, K. J.; O'Dell, L. A.; Schurko, R. W. Ultra-wideline ^{14}N solid-state NMR as a method for differentiating polymorphs: glycine as a case study. *CrystEngComm* **2015**, *17*, 5225–5236.

(52) Veinberg, S. L.; Friedl, Z. W.; Lindquist, A. W.; Kispal, B.; Harris, K. J.; O'Dell, L. A.; Schurko, R. W. ^{14}N solid-state NMR spectroscopy of amino acids. *ChemPhysChem* **2016**, *17*, 4011–4027.

(53) Veinberg, S. L.; Johnston, K. E.; Jaroszewicz, M. J.; Kispal, B. M.; Mireault, C. R.; Kobayashi, T.; Pruski, M.; Schurko, R. W. Natural abundance ^{14}N and ^{15}N solid-state NMR of pharmaceuticals and their polymorphs. *Phys. Chem. Chem. Phys.* **2016**, *18*, 17713–17730.

(54) O'Dell, L. A.; Schurko, R. W. Static solid-state ^{14}N NMR and computational studies of nitrogen EFG tensors in some crystalline amino acids. *Phys. Chem. Chem. Phys.* **2009**, *11*, 7069–7077.

(55) Harris, K. J.; Veinberg, S. L.; Mireault, C. R.; Lupulescu, A.; Frydman, L.; Schurko, R. W. Rapid acquisition of ^{14}N solid-state

- NMR spectra with broadband cross polarization. *Chem. - Eur. J.* **2013**, *19*, 16469–16475.
- (56) Schurko, R. W. Ultra-wideline solid-state NMR spectroscopy. *Acc. Chem. Res.* **2013**, *46*, 1985–1995.
- (57) O'Dell, L. A.; Schurko, R. W. Fast and simple acquisition of solid-state ^{14}N NMR spectra with signal enhancement via population transfer. *J. Am. Chem. Soc.* **2009**, *131*, 6658–6659.
- (58) O'Dell, L. A.; Schurko, R. W.; Harris, K. J.; Autschbach, J.; Ratcliffe, C. I. Interaction tensors and local dynamics in common structural motifs of nitrogen: a solid-state ^{14}N NMR and DFT study. *J. Am. Chem. Soc.* **2011**, *133*, 527–546.
- (59) O'Dell, L. A.; Ratcliffe, C. I.; Kong, X.; Wu, G. Multinuclear solid-state nuclear magnetic resonance and density functional theory characterization of interaction tensors in taurine. *J. Phys. Chem. A* **2012**, *116*, 1008–1014.
- (60) Holmes, S. T.; Schurko, R. W. Refining crystal structures with quadrupolar NMR and dispersion-corrected density functional theory. *J. Phys. Chem. C* **2018**, *122*, 1809–1820.
- (61) Holmes, S. T.; Iuliucci, R. J.; Mueller, K. T.; Dybowski, C. Semi-empirical refinements of crystal structures using ^{17}O quadrupolar-coupling tensors. *J. Chem. Phys.* **2017**, *146*, 064201.
- (62) Holmes, S. T.; Vojvodin, C. S.; Schurko, R. W. Dispersion-corrected DFT methods for applications in nuclear magnetic resonance crystallography. *J. Phys. Chem. A* **2020**, *124*, 10312–10323.
- (63) Holmes, S. T.; Engl, O. G.; Srncic, M. N.; Madura, J. D.; Quiñones, R.; Harper, J. K.; Schurko, R. W.; Iuliucci, R. J. Chemical shift tensors of cimetidine form A modeled with density functional theory calculations: implications for NMR crystallography. *J. Phys. Chem. A* **2020**, *124*, 3109–3119.
- (64) Fischer, M. S.; Templeton, D. H.; Zalkin, A. Solid state structure and chemistry of the choline halides and their analogues. redetermination of the betaine hydrochloride structure $[(\text{CH}_3)_3\text{NCH}_2\text{COOH}]^+\text{Cl}^-$. *Acta Crystallogr., Sect. B: Struct. Crystallogr. Cryst. Chem.* **1970**, *26*, 1392–1397.
- (65) Santarsiero, B. D.; Marsh, R. E. N, N-Dimethylglycine hydrochloride. *J. Crystallogr. Spectrosc. Res.* **1983**, *13*, 245–251.
- (66) He, Y.-J.; Zou, P.; Wang, H.-Y.; Wu, H.; Xie, M.-H. Glycine ethyl ester hydrochloride. *Acta Crystallogr., Sect. E: Struct. Rep. Online* **2010**, *66*, No. o2115.
- (67) Mishiro, K.; Hu, F.; Paley, D. W.; Min, W.; Lambert, T. H. Macrosteres: the deltic guanidinium ion. *Eur. J. Org. Chem.* **2016**, *2016*, 1655–1659.
- (68) Harrison, W. T. A.; Yathirajan, H. S.; Narayana, B.; Sreevidya, T. V.; Sarojini, B. K. Redetermination of e-D-glucosamine hydrochloride: elucidation of the hydrogen-bonding scheme. *Acta Crystallogr., Sect. E: Struct. Rep. Online* **2007**, *63*, No. o3248.
- (69) Dittrich, B.; Munshi, P.; Spackman, M. A. Redetermination, invariom-model and multipole refinement of L-ornithine hydrochloride. *Acta Crystallogr., Sect. B: Struct. Sci.* **2007**, *63*, 505–509.
- (70) Bryndal, I.; Jaremko, M.; Jaremko, L.; Lis, T. Comparison of the methyl ester of L-tyrosine hydrochloride and its methanol monosolvate. *Acta Crystallogr., Sect. C: Cryst. Struct. Commun.* **2006**, *62*, No. o111.
- (71) Ambady, G.; Kartha, G. Crystal structure and absolute configuration of yohimbine hydrochloride, $\text{C}_{21}\text{H}_{27}\text{ClN}_2\text{O}_3$. *J. Cryst. Mol. Struct.* **1973**, *3*, 37–45.
- (72) Bruno, I. J.; Cole, J. C.; Edgington, P. R.; Kessler, M.; Macrae, C. F.; McCabe, P.; Pearson, J.; Taylor, R. New software for searching the Cambridge Structural Database and visualizing crystal structures. *Acta Crystallogr., Sect. B: Struct. Sci.* **2002**, *58*, 389–397.
- (73) O'Dell, L. A.; Schurko, R. W. QCPMG using adiabatic pulses for faster acquisition of ultra-wideline NMR spectra. *Chem. Phys. Lett.* **2008**, *464*, 97–102.
- (74) O'Dell, L. A.; Rossini, A. J.; Schurko, R. W. Acquisition of ultra-wideline NMR spectra from quadrupolar nuclei by frequency stepped WURST-QCPMG. *Chem. Phys. Lett.* **2009**, *468*, 330–335.
- (75) Bhattacharyya, R.; Frydman, L. Quadrupolar nuclear magnetic resonance spectroscopy in solids using frequency-swept echoing pulses. *J. Chem. Phys.* **2007**, *127*, 194503.
- (76) Kupce, E.; Freeman, R. Adiabatic pulses for wideband inversion and broadband decoupling. *J. Magn. Reson., Ser. A* **1995**, *115*, 273–276.
- (77) Kentgens, A. P. M. A practical guide to solid-state NMR of half-integer quadrupolar nuclei with some applications to disordered systems. *Geoderma* **1997**, *80*, 271–306.
- (78) Bryce, D. L.; Sward, G. D. Solid-state NMR spectroscopy of the quadrupolar halogens: chlorine-35/37, bromine-79/81, and iodine-127. *Magn. Reson. Chem.* **2006**, *44*, 409–450.
- (79) van Meerten, S. G. J.; Franssen, W. M. J.; Kentgens, A. P. M. ssNake: a cross-platform open-source NMR data processing and fitting application. *J. Magn. Reson.* **2019**, *301*, 56–66.
- (80) Massiot, D.; Farnan, L.; Gautier, N.; Trumeau, D.; Trokiner, A.; Coutures, J. P. ^{71}Ga and ^{69}Ga nuclear magnetic resonance study of $\beta\text{-Ga}_2\text{O}_3$: resolution of four- and six-fold coordinated Ga sites in static conditions. *Solid State Nucl. Magn. Reson.* **1995**, *4*, 241–248.
- (81) Medek, A.; Frydman, V.; Frydman, L. Central transition nuclear magnetic resonance in the presence of large quadrupole couplings: cobalt-59 nuclear magnetic resonance of cobaltphthalocyanines. *J. Phys. Chem. A* **1999**, *103*, 4830–4835.
- (82) Eichele, K.; Wasylishen, R. E. *WSolidsI: Solid-State NMR Spectrum Simulation*, version 1.17.30; University of Tubingen: Tubingen, 2001.
- (83) Hammer, B.; Hansen, L. B.; Nørskov, J. K. Improved adsorption energetics within density-functional theory using revised Perdew-Burke-Ernzerhof functionals. *Phys. Rev. B: Condens. Matter Mater. Phys.* **1999**, *59*, 7413–7421.
- (84) Grimme, S. Semiempirical GGA-type density functional constructed with a long-range dispersion correction. *J. Comput. Chem.* **2006**, *27*, 1787–1799.
- (85) Pfrommer, B. G.; Côté, M.; Louie, S. G.; Cohen, M. L. Relaxation of crystals with the quasi-Newton method. *J. Comput. Phys.* **1997**, *131*, 233–240.
- (86) Pickard, C. J.; Mauri, F. All-electron magnetic response with pseudopotentials: NMR chemical shifts. *Phys. Rev. B: Condens. Matter Mater. Phys.* **2001**, *63*, 245101.
- (87) Adiga, S.; Aebi, D.; Bryce, D. L. EFGShield — a program for parsing and summarizing the results of electric field gradient and nuclear magnetic shielding tensor calculations. *Can. J. Chem.* **2007**, *85*, 496–505.
- (88) Pyykkö, P. Year-2017 nuclear quadrupole moments. *Mol. Phys.* **2018**, *116*, 1328–1338.
- (89) O'Dell, L. A.; Harris, K. J.; Schurko, R. W. Optimized excitation pulses for the acquisition of static NMR powder patterns from half-integer quadrupolar nuclei. *J. Magn. Reson.* **2010**, *203*, 156–166.
- (90) Altenhof, A. R.; Lindquist, A. W.; Foster, L. D. D.; Holmes, S. T.; Schurko, R. W. On the use of frequency-swept pulses and pulses designed with optimal control theory for the acquisition of ultra-wideline NMR spectra. *J. Magn. Reson.* **2019**, *309*, 106612.
- (91) Koppe, J.; Hansen, M. R. Minimizing lineshape distortions in static ultra-wideline nuclear magnetic resonance of half-integer spin quadrupolar nuclei. *J. Phys. Chem. A* **2020**, *124*, 4314–4321.
- (92) Altenhof, A. R.; Jaroszewicz, M. J.; Lindquist, A. W.; Foster, L. D. D.; Veinberg, S. L.; Schurko, R. W. Practical aspects of recording ultra-wideline NMR patterns under magic-angle spinning conditions. *J. Phys. Chem. C* **2020**, *124*, 14730–14744.
- (93) Lupulescu, A.; Kotecha, M.; Frydman, L. Relaxation-assisted separation of chemical sites in NMR spectroscopy of static solids. *J. Am. Chem. Soc.* **2003**, *125*, 3376–3383.
- (94) Jaroszewicz, M. J.; Frydman, L.; Schurko, R. W. Relaxation-assisted separation of overlapping patterns in ultra-wideline NMR spectra. *J. Phys. Chem. A* **2017**, *121*, 51–65.
- (95) Tatton, A. S.; Pham, T. N.; Vogt, F. G.; Iuga, D.; Edwards, A. J.; Brown, S. P. Probing intermolecular interactions and nitrogen protonation in pharmaceuticals by novel ^{15}N -edited and 2D ^{14}N - ^1H solid-state NMR. *CrystEngComm* **2012**, *14*, 2654–2659.
- (96) Tatton, A. S.; Pham, T. N.; Vogt, F. G.; Iuga, D.; Edwards, A. J.; Brown, S. P. Probing hydrogen bonding in cocrystals and amorphous

dispersions using ^{14}N - ^1H HMQC solid-state NMR. *Mol. Pharmaceutics* **2013**, *10*, 999–1007.

(97) Oja, T. Nitrogen-14 nuclear quadrupole resonance study of the guanidinium ion. *J. Chem. Phys.* **1973**, *59*, 2668–2675.

(98) Krause, L.; Whitehead, M. A. ^{14}N pure quadrupole resonance in some five-membered heterocyclic compounds and in three acyclic compounds. *Mol. Phys.* **1973**, *25*, 99–111.

(99) Chen, C.-H.; Dodgen, H. W. Nuclear quadrupole resonance of nitrogen-14 in guanidine complexes, cyanoguanidine, and substituted ureas. *J. Magn. Reson.* **1976**, *22*, 139–147.